ZEOLITE TEMPLATED CARBONS: INVESTIGATIONS IN EXTREME TEMPERATURE ELECTROCHEMICAL CAPACITORS AND LEAD-ACID BATTERIES

A Thesis
Presented to
The Academic Faculty

by

Yair Korenblit

In Partial Fulfillment
of the Requirements for the Degree
PhD in the
School of Materials Science and Engineering

Georgia Institute of Technology
May, 2012

ZEOLITE TEMPLATED CARBONS: INVESTIGATIONS IN EXTREME TEMPERATURE ELECTROCHEMICAL CAPACITORS AND LEAD-ACID BATTERIES

Approved by:
Dr. Gleb Yushin, Advisor
School of Materials Science and Engineering
Georgia Institute of Technology

Dr. David Bucknall, Co-advisor
School of Materials Science and Engineering
Georgia Institute of Technology

Dr. Alexander Alexeev
School of Mechanical Engineering
Georgia Institute of Technology

David Mihara
Senior Director, Advanced Materials & Processes
Exide Technologies

Dr. Sudhakar Jagannathan
Senior Materials Scientist, Advanced Materials & Processes
Exide Technologies
Date Approved: March 22, 2012

With immense gratitude to my parents, Simcha, Gil, Liat, extended family, Jane, and friends whose support and impact are beyond measure.

ACKNOWLEDGEMENTS

I wish to thank Dr. Gleb Yushin for introducing me to the intriguing field of energy storage and many other aspects of science and technology including, but not limited to, carbon materials, lithium-ion batteries, supercapacitors, start-up companies, proposal and grant writing, and so much more. You have truly changed the course of my life. I cannot thank enough Dr. Lawrence Bottomley, Dr. Sam Colgate, Dr. Paul Kohl, Dr. Tom Fuller, Dr. Brent Carter, and Dr. David Bucknall for having invested so much time, effort, and care in the education of future scientists and engineers. Their courses stand out vividly amongst the many courses I have attended as part of my university studies. I would like to thank my family, friends and co-workers, for all the great support that they provided, without which I would have not been able to complete this body of work. You all have assisted me in living a very full life while chipping away at the milestones of this doctorate of philosophy. In addition to those mentioned in my dedication, I would like to thank Ken and Rachel Beyerlein, Rollo Gittens, Kim Portmess, Janeen Hicks, John Goldin, Dan Hurwitz et al., Ben Johnstone, Summer McLane, Cantwell Carson, Desiree Jennings, Lex Nunnery, Donald Duchemin, Rob Maggio, Hannah Bowles, Matt Clark, the volleyball and frisbee crews, and so many other colorful characters who have enriched my life. Exide Technologies has been extremely generous in assisting me to meet my goals professionally and academically. Exide has provided me with an educational exposure to lead-acid batteries, their research and development, and various other technologies and research efforts. I would like to thank Paul Cheeseman, David Mihara, Sudhakar Jagannathan, Hope Wittke, Bill Murray, David Atherton, Frank Malo, Ibrahim, William, Prosper, Chris, Cris, Mort, Cassandray,

Brandy, Ronnie, and so many others at Exide who have contributed significantly to my research efforts and experiences. The TI:GER program also has had a vast influence on my outlook and my exposure to the fields of entrepreneurship, business and law. This program provided some of the most diverse educational aspects of my academic career. Finally, I would like to thank my lab mates, including Adam Kajdos who contributed significantly to the work in this thesis, Ben Hertzberg, Kara Evanoff, Jim Benson, Igor Kovalenko, Alexander Magasinski, Patrick Dixon, and many others who taught me and exposed me to many different aspects of research and life in general.

TABLE OF CONTENTS

LIST OF TABLES

LIST OF FIGURES

LIST OF SYMBOLS AND ABBREVIATIONS

EDLC	Electrochemical double-layer capacitor
EC	Electrochemical capacitor
CVD	Chemical vapor deposition
LPCVD	Low pressure chemical vapor deposition
CDC	Carbide-derived carbon
DFT	Density functional theory
NLDFT	Non-local Density functional theory
BET	Brunnauer, Emmet, and Teller
VRLA	Valve-regulated lead-acid
PAM	Positive active material
NAM	Negative active material
$PbSO_4$	Lead sulfate
PbO_2	Lead dioxide
Pb	Lead
AN	Acetonitrile
MF	Methyl formate
MA	Methyl acetate
DIOX	1,3 dioxolane
SBP-BF4	Spiro-(1,1')-bipyrrolidinium tetrafluoroborate
$TEABF_4$	Tetraethylammonium tetrafluoroborate
SSA	Specific surface area
m^2/g	Meters squared per gram

HEV	Hybrid-electric vehicle
$/kJ	Dollars per kilojoule
C	Capacitance
Q or q	Charge
V	Voltage
ε_0	Permittivity of free space
ε_r	Relative dielectric constant
A	Area
d	Distance
F	Force
G	Free energy
r	Distance
λ	Fraction of charge
dG	Change in free energy
dq	Differential charge
$d\lambda$	Differential fraction
F	Farads
g^{-1}	Per gram
dv/dt	Voltage sweep rate, volts per second
R	Resistance
I	Current in amps
Wh/kg	Watt-hours per kilogram
W/kg	Watts per kilogram
KOH	Potassium hydroxide
$ZnCl_2$	Zinc chloride

H_3PO_4	Phosphoric acid
H_2SO_4	Sulfuric acid
°C	Degrees Celsius
°F	Degrees Fahrenheit
F/g	Farads per gram
CNT	Carbon nanotubes
MWCNT	Multi-walled carbon nanotubes
2D	Two-dimensional
3D	Three-dimensional
RuO_2	Ruthenium oxide
e^-	Electron
ZTC	Zeolite-templated carbon
ZCC	Zeolite-carbon composite
FZCC	Functionalized zeolite-carbon composite
C	Carbon
Ar	Argon
TEM	Transmission electron microscope
C-D	Charge-discharge
A/g	Amps per gram
Ah/kg	Amp-hours per kilogram
ESR	Equivalent series resistance
kg	Kilograms
J	Joules
CV	Cyclic voltammetry
EIS	Electrochemical Impedance Spectroscopy

f	Frequency
Z”	Imaginary component of the impedance
Z’	Real component of the impedance
C’	Real component of the capacitance
C”	Imaginary component of the capacitance
τ_o	Time constant
ω	Angular frequency
f_{trans}	Transition frequency
Hz	Hertz
K	Kelvin
N_2	Nitrogen gas
CO_2	Carbon dioxide gas
nm	Nanometer
P	Pressure
V_a	Volume of gas adsorbed
CO_2	Carbon dioxide gas
XRD	X-ray diffraction
SEM	Scanning-electron microscopy
PTFE	Polytetrafluoroethylene
wt. %	Weight percent
µm	Micrometers
ppm	Parts per million
kHz	Kilohertz
mV	Millivolts
PSD	Particle size distribution

mg	Milligrams
mA/g	Milliamps per gram
LAB	Lead-acid battery

SUMMARY

Porous carbons are versatile materials with applications in different fields. They are used in filtration, separation and sequestration of fluids and gases, as conductive additives in many energy storage materials, as coloring agents, as pharmaceutical and food additives, and in many other vital technologies. Porous carbons produced by pyrolysis and activation of organic precursors commonly suffer from poorly controlled morphology, microstructure, chemistry, and pore structure. In addition, the poorly controlled parameters of porous carbons make it challenging to elucidate the underlying key physical parameters controlling their performance in energy storage devices, including electrochemical capacitors (ECs) and lead-acid batteries (LABs). Zeolite-templated carbons (ZTCs) are a novel class of porous carbon materials with uniform and controllable pore size, microstructure, morphology, and chemistry. In spite of their attractive properties, they have never been explored for use in LABs and their studies for ECs have been very limited. Here I report a systematic study of ZTCs applications in ECs operating at temperatures as low as - 70 ˚C and in LABs. Greatly improved power and energy performance, compared to state of the art devices, has been demonstrated in the investigated ECs. Moreover, the application of ZTCs in LABs has resulted in a dramatic enhancement of their cycle life and power and energy densities.

CHAPTER 1

INTRODUCTION

1.1 Motivation

There is a variety of energy sources that are of importance to mankind. These include the sun, wind, fuels such as hydrogen, oxygen, methane, the heat emanating from the core of our earth, the waves in our oceans, the flow of our rivers, and various other easily perceived and more salient sources of energy. In our attempts to harness this energy for our benefit, it has become apparent that there are situations in which the ability to capture this energy for later use is of great utility, for example, when using wind energy as a source for electrical energy in our grid. The peak usage times of our electricity may not be congruent with peak wind flow. This would imply that if we had a means to store that energy for use when peak demand was higher, we could better utilize renewable energy.

The population of the earth is growing along with their energy demands. Despite their possible inaccuracy as to the rate or quantity, predictions concerning these facts provide impetuses for the important work that must be done to utilize different energy sources for humanity's benefit. One such estimate, provided by The World Energy Outlook 2004, projects that by the year 2060 the world's energy demand will increase by 60% [1]. In addition, society's heavy reliance on hydrocarbon fuels has been associated with a detrimental impact on the environment. Just these few notions are sufficient to provide motivation for the important work needed to be done to expand our technological capabilities. It is very likely that our ability to mediate these developing problems lies in

the development of technologies to alleviate the reliance on hydrocarbon fuels and to expand our toolbox of energy sources and energy storage technologies.

There are many other goals and obstacles that need to be addressed. Developing countries are facing increasing demands of energy for transportation, industrial needs, and a variety of other applications. Increasing demands are being made on electronic devices and electrical machines. For instance, hybrid/electric vehicles (HEV/EV) are seeing increased power demands from consumers. An increasing amount of power-draining loads and population result in problems of power quality and level maintenance. Maintaining the voltage levels and preventing what is known as voltage sags has been found to be the most common electrical disturbance in distribution systems [2]. Electrochemical energy storage technologies have been pegged as potential technologies with the capacity to alleviate some of these growing concerns [3]. Two particular systems of interest are electrochemical capacitors (ECs) and lead-acid batteries (LABs). These two systems have shown promise in a variety of areas (e.g., renewable energy, HEV, load-leveling) [4-10] mentioned above, and their advancement is of vital interest to society.

ECs are often defined as electrochemical energy storage devices with performance characteristics, with respect to energy and power density, that lie between solid-state capacitors and batteries. Their performance can be roughly contrasted with various energy storage technologies using a Ragone plot such as the one in figure 1.1.

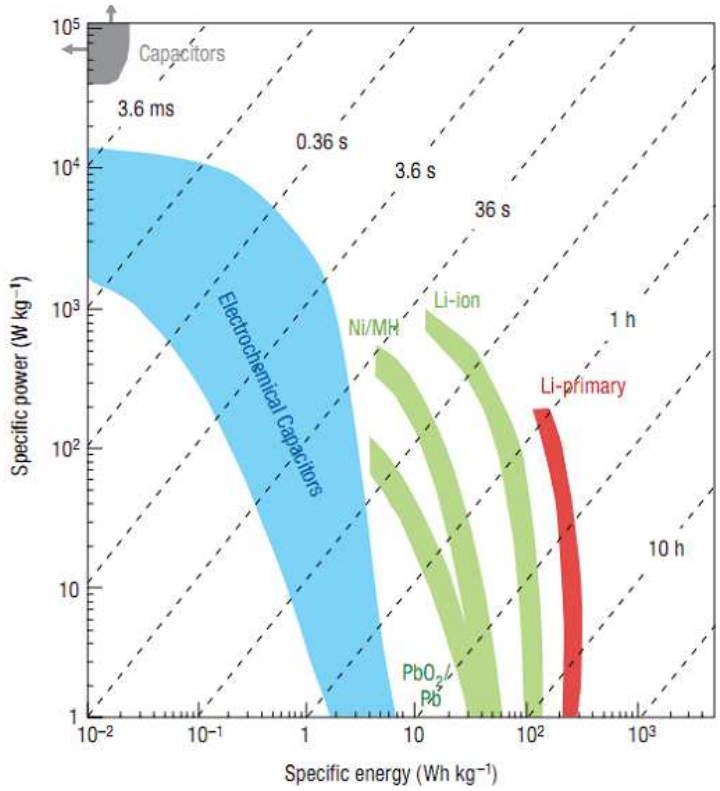

Figure 1.1. Ragone plot comparing energy and power performance for a variety of systems and the gradients within them [11].

ECs are manufactured by many companies, including Maxwell Technologies (US), ESMA (Russia), Elit (Russia), Tavrima (Canada), Panasonic (Japan), Ness Capacitor (South Korea), Epcos (South Korea), LG (South Korea), and Samsung (South Korea). The ability of ECs to provide a combination of fairly high energy and power densities (figure 1.1) opens a broad range of applications. A cost comparison of dollars per kilojoule ($/kJ) in 2001 suggests that while batteries were able to provide energy at nearly thirteen times lower cost per kJ than an EC, the power (energy delivered per unit time) of batteries was three times more expensive [12].

In order to increase the utilization of ECs, enhancements to the energy density and range of operating temperature are necessary. For example, in many applications it is

desirable to couple ECs with batteries, but in order to do so both must have the same temperature operating capabilities. In addition, there are many applications requiring extreme temperature operations such as the Air Force's More Electric Initiative (MEI) [13].

Momentum has been increasing significantly over the past decade with respect to what is perceived by many to be an established chemistry - LABs. LABs were invented in the 19th century but the changes in the demands on these storage devices results in changes in their behavior that requires new materials and much research into their operation and failure mechanisms. In addition, despite their utilization over many decades, commercial batteries still fail to use the active material to a significant fraction of its theoretical density of around 167 Wh/kg [14, 15]. Results vary, but to date it appears that standard LABs utilize less than a 1/3 of their theoretical density (30-50 Wh/kg [15]). The importance of LABs' continued advancement, despite the higher energy density of lithium-ion (> 100 Wh/kg [11]) and nickel-metal hydride (60-70 Wh/kg [15]) battery systems, lies in their established recycling infrastructure, robustness, and low cost of materials and production. The latter characteristics have secured LABs position as the battery for use in starting, lighting and ignition (SLI) for roughly a century.

Much research is underway in Li-ion and NiMH chemistries in order to facilitate their utilization in hybrid-electric vehicles (HEVs). Despite the lower energy densities of LABs, by improving their performance there is a place for LABs in electric vehicles, from very mild to full electric vehicles. Wheego Electric Cars, Inc. is already using LABs in their 25 MPH-limited electric vehicles. In addition to the use of LABs in mobile applications, their use in stationary applications is appealing due to their cost.

In order to facilitate the use of LABs in HEVs, their design must change. This is because using a LAB for SLI functions is very different from using it for HEVs, which often requires the LAB to operate in a partial-state of charge (PSOC) and accept and provide high currents at such a state for many cycles. This operation often results in a build-up of lead sulfate ($PbSO_4$) on the anode causing it to fail (sulfation). The two main causes attributed to the failure of the anode is prevention of the electrolyte to reach the active surface by insulating lead sulfate and isolation of active material from the current source by lead sulfate [16]. To address these issues, research efforts have varied from adding multiple lugs to the plates in order to distribute the potential more evenly [17] to using conductive and non-conductive additives [18-20]. In order to better understand the design needs of these additives and to create anode materials that can withstand HRPSOC and increased cyclability, further research into these additives is necessary.

Improving LABs and ECs will likely lead to the enhancement of the lives of individuals around the world and potentially improve the health of the environment. Future and current applications which could benefit from these enhancements include memory backup, energy efficient hybrid engines, electric vehicles, high power electric tools, and power quality. Many of these applications are currently feasible yet are stymied by the shortcomings of these systems' ability to withstand the needs of their applications. Through continued research and investigation of various synthesis methods and materials, improved performance can be facilitated while providing scientists enhanced insight into the underlying mechanisms and result in the incorporation of these storage devices into many commercial and military technologies [21].

1.2 Historical Perspective

1.2.1 The History of Zeolite-Templated Carbon

The first few studies into the decomposition of organic compounds in the 3D pore structure of zeolite took place in the early 1990's [22]. These studies were presented to the public in 1992 by Kyotani et al. (reference 8 in reference 22), Enzel et al. [23, 24], and Cordero et al. [25]. Kyotani et al.'s work involved the decomposition of poly(furfuryl alcohol) in the pores of zeolite and the formation of porous carbon. Enzel et al. decomposed poly(acrylonitrile) (PAN) and removed the template with HF. Cordero decomposed propylene over the zeolite followed by HF and HCl substrate removal and demonstrated significant to total removal of the zeolite through XRD. Enzel studied the surface functionalities and found a large fraction of nitrogen surface groups (N/C ratios of ~0.18-0.2) and that the NaY zeolite may act to prohibit significant graphitization of the carbon within the zeolite pores (via FTIR), attributing it to the low conductivity (2E-5 S/cm) found for their PAN-derived ZTC. In 1997 Kyotani et al. published an article geared towards expanding the knowledge on carbons created by decomposition within zeolites followed by removal of their templates. The paper was meant to call attention to the porous carbon synthesized through this method and its properties, such as uniform 3D pore structure conferred by the zeolite and has since been cited over 240 times [22]. These investigations laid the foundation for the synthesis, study, and application of microporous ZTC, which will be described in following sections.

1.2.2 The History of Electrochemical Capacitors

In 1957 Becker patented an energy storage device based on a porous carbon utilizing an aqueous electrolyte, an electrochemical capacitor [26]. In 1966 the Sohio

Corporation in Cleveland, Ohio created a similar device utilizing a non-aqueous solution that permitted higher operating voltages and, thus, higher energy densities [27]. In 1971 Trasatti et al. reported the interesting capacitance performance of an expensive metal oxide, ruthenium oxide [28]. In 1975 B. E. Conway used Faradaic reactions and the potential dependence of electrochemical adsorption of monolayers of base metals such as lead, bismuth, and copper on noble metals and the redox reactions associated with ruthenium oxide in sulfuric acid to create significantly higher energy density electrochemical capacitors as compared to that designed by Becker's carbon electrochemical capacitor [29].

Becker's technology and that of those who followed him relied on a physical phenomenon that was first investigated half a century earlier by Hermann von Helmholtz [30]. These storage devices are now known as electrochemical capacitors, supercapacitors, and ultracapacitors. The mechanism allowing for their energy storage is that of the double layer or the double layer combined with surface redox reactions (mostly in aqueous solutions with metal oxide electrodes). The double layer arises in all solid/electrolyte interfaces and phase boundaries between two immiscible electrolyte solutions.

Helmholtz modeled the distribution of ions near the surface of the electrode. His model described charge on one side of the electrode separated by several nanometers from the opposing charges provided by the dense layer of solution ions in which the electrode is immersed. The foundation for this model lay in the operating principles of the parallel plate capacitor. In truth, the phenomenon of charge storage at a surface was not new in Helmholtz's time, either. Static charge on the face of amber was acknowledged during ancient times and the scientific studies from that era to modern

times were necessary to decipher the mechanisms underlying the operation of electrochemical capacitors. Studies had to be undertaken in the molecular theory of electricity, the electron theory of metals, solvation, diffusion, and electrical and ionic conduction. The major bodies of work to uncover these mechanisms entailed the research of Michael Faraday, Joseph John Thompson, and Robert Andrews Millikan. Through their work our understanding of parallel plate capacitors and the Leyden jar was made possible. The Leyden jar, attributed to Ewald Jurgens von Kleist and Pieter van Musschenbroek from Leyden, was a glass jar in which was an aqueous electrolyte that had an immersed electrode and on the outside a metal foil. The jar allowed for charge storage and separation via a glass dielectric. It was later known as a "condenser," and finally as a capacitor. Eventually, other dielectrics were used such as air, vacuum, polystyrene, mica, and many other materials.

Following the original work of Helmholtz, Gouy and Chapman had considered that the thermal motion of the ions in solution would lead to a diffuse layer of adsorbed ions, rather than a dense layer as described in Helmholtz's original treatise. After Gouy and Chapman's work, Stern then provided a modification that took into account the fact that ions in solution are not ideal point charges and allowed them to have volume. As a result, the center of the ions resided at a distance from the metal (electrode) surface while utilizing the distribution modeled by Gouy and Chapman. The last fundamental modification to this developed theory was made by Grahame in 1947. Grahame used the information gained from studying the structure of the electrolyte to elucidate that the metal/solution interaction leads to different planes of closest approach for the ions depending on their solvation-state and surface interaction. This finalized the Gouy-

Chapman-Stern-Grahame model of the electrical double layer, the qualitative model most accepted for the description of this phenomenon. As time progressed, further enhancements were made by theoreticians to adjust for realizations made with time that were not available to the ground-breaking researchers who came before them. It is worth noting that in many instances technology comes before a deep understanding of theory is available, but in the case of electrochemical capacitors, it was the theory that propagated the advancement and proliferation of the technology [29].

1.2.3 The History of Lead-acid Batteries

In 1854, German physicist Wilhelm Josef Sinsteden created a system that could accept charge, release it when necessary, and could then be charged again. Today such a system would be known as a rechargeable battery, or a secondary battery. He built this system by using two large lead plates in diluted sulfuric acid. Upon repeated charging and discharging the cell gave measurable capacity (or ability to accept charge and store it till discharge). In 1859 a French scientist brought to the world a secondary battery that would surpass all rechargeable batteries that came prior. Gaston Planté employed a pair of spirally wound, or rolled, lead plates separated by rubber strips in dilute sulfuric acid. Rolling the plate provided for an increased area of plates to be employed in the chemical reactions and the rubber prevented the electrical contact of the positive and negative electrodes while allowing for their close proximity. Primary cells were used to charge the battery for 24 hours. The positive plate formed a brown coating of PbO_2 and evolved oxygen while the negative electrode left the pure lead unchanged and evolved hydrogen. In 1879 he published a book discussing his work on high voltage power sources and

secondary batteries [31]. Examples of his designs for spiral LABs and parallel-plate LABs are shown in figure 1.2.

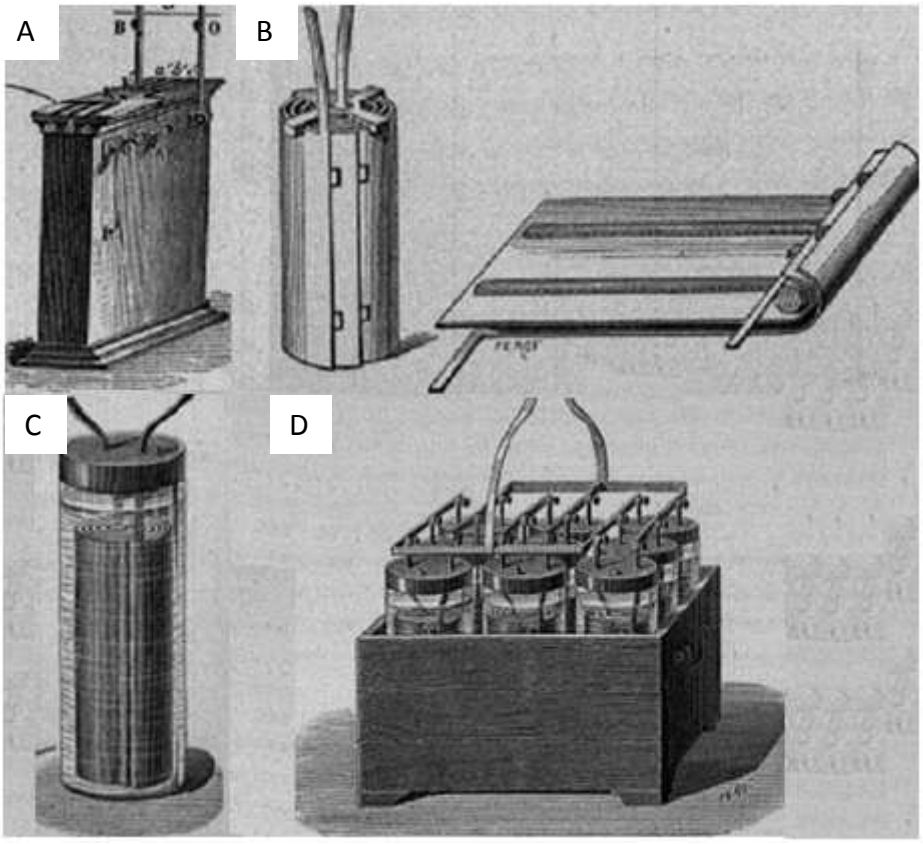

Figure 1.2. Parallel-plate (A) and spiral (B-D) LABs as devised by Planté [31].

The early applications of Planté's accumulators included heating platinum wires for surgery and dentistry, miner's electric lamps, electric bells and horns, signals for ships, and electric brakes for steam trains. His battery was premature in the sense that in order to charge his accumulators Bunsen and Daniell cells were required. In 1873 the Gramme machine (built by Zénobe Théophile Gramme) was demonstrated in a Vienna exhibition. Gramme made direct-current generators and in conjunction Planté demonstrated the ability of his LAB to run the generator reversibly as an engine. The Breguet Company then began to manufacture Plant's first commercial storage batteries [31].

In 1880-81 Camille Alphonse Faure achieved high capacities by coating the electrode with sulfur-containing lead powder pastes that were then formed into PbO_2 and spongy Pb. In 1881 J. Scudamore Sellon applied lead paste to a perforated thin metal plate of lead-antimony (for strengthening the grid-other researchers had done the same) that increased adhesion of the active paste. In 1881, Gustave Trouve powered a three-wheeled electric vehicle by a LAB. In 1891 a LAB-based electric submarine was launched. The telegraph and telephone companies along with the light bulb demanded the deployment of batteries on a large scale. Planté's plates competed with Faure's pasted plates till the first decade of the 20th century, but Faure's design provided higher performance in many applications. Nevertheless, Planté's batteries are still constructed to this day in smaller volume [31].

Near the turn of the 19th century, batteries helped eliminate the need to hand-crank engines and provide ignition and lighting. When DC-generators came along they were used to charge the car batteries and supply power during engine operation. In the 1960's increased loads demanded an increase to 14V for the electrical vehicle system and replace DC generators with 3-phase alternators. The increase in power demand on the vehicle's system (figure 1.3) means that when demand exceeds alternator output, the car battery must then supply power [32]. Despite these changes, the car battery's responsibilities did not change for many decades. The increased power demands required the LAB industry to provide improved materials, at a lower cost, and with time, design changes.

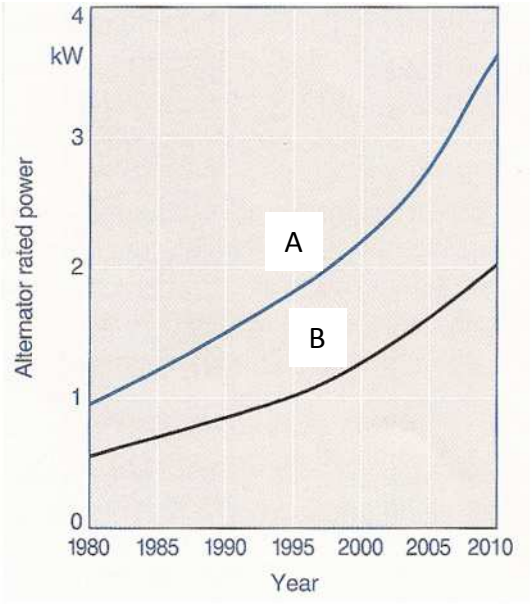

Figure 1.3. Alternator rated power as a function of time, reflecting the increasing demands on LABs employed in (A) luxury cars, and (B) intermediate-sized cars [32].

Shortly after World War II sealed Ni-Cd batteries appeared on the market with immobilized electrolyte. Prior to that time LABs would experience a loss of water due to hydrogen and oxygen evolution and were not sealed, leading to the possibility of electrolyte escape from the battery. The inspiration from the Ni-Cd batteries using fiber felt came in the form of a gel formation by combining fumed silica with acid. In the 1950's SONNENSCHEIN batteries became the first valve-regulated lead-acid (VRLA) batteries based on immobilization of the electrolyte. The valve allowed for release of gases when the pressure was excessive and these batteries were initially sold in small capacity formats. In the 1970's micron glass fibers (designed for air filters) appeared on the market and showed promise of acid affinity and Pb dendrite growth prevention. The adsorbent glass matt (AGM) separator was used initially in the wound cell format, and then larger prismatic cells appeared for stationary applications. VRLA batteries based on gel and AGM are sold to this day [33].

1.3 Principles of Operation

1.3.1 Capacitors

The following sections provide a description of the physical processes underlying the operation of electrochemical capacitors. Since the inspiration for the model given by Helmholtz came from the understanding of parallel-plate capacitors, or electrostatic solid-state capacitors, that technology will be used as a starting point for the explanation of electrochemical capacitor operation.

1.3.1.1 Parallel-Plate Capacitors

The most common electrostatic capacitors are generally constructed out of two metal plates, separated by vacuum or dielectric materials, such as air, water, barium titanate, or silicon dioxide [34]. Figure 1.4 shows a simplified response of the dielectric material and a generalized setup for a solid-state parallel-plate capacitor under bias.

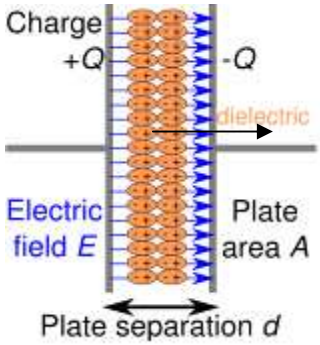

Figure 1.4. Solid-state capacitor [35].

When the bias is removed, the charge/energy is stored, and upon closing of the circuit the energy is released, mainly in the form of electric current flow. The ability of the system to store charge upon application of a potential is a measure of its capacitance

(not to be mistaken for a battery's ability to store charge – known as capacity). Capacitance (C) is defined as follows

$$C = \frac{Q}{V} \text{ (farads)} \qquad (1.1)$$

$$C = \varepsilon_o \varepsilon_r \frac{A}{d} \text{ (farads)} \qquad (1.2)$$

Q is the amount of charge (coulombs) on one plate and V (volts) is the potential difference applied to the two plates. The unit of capacitance is a farad which is equivalent to coulombs per volt. The capacitance can also be determined by the area of the plates (A), multiplied by the relative dielectric constant (ε_r, unitless), also known as the relative static permittivity of the material between the plates. This is multiplied by the permittivity of free space (ε_0 - 8.85×10^{-12} F/m based on using meters for the plate distance and area), divided by the distance between the plates (d). The key factors for performance control in such a device are the distance between the plates, the dielectric constant, and the area of the plates [29, 30]. The relative permittivity factor represents the ability of the material to transmit an electric field and is affected by the behavior of the material under a polarizing field [29]. As the material is subjected to the electric field, it has several polarization mechanisms that may take place, which include electronic, ionic, dipolar, and space charge polarizations. These mechanisms are frequency dependent (see figure 1.5) and may be pronounced in different amounts in different materials, for instance polar liquids have more tendency to reorient than non-polar liquids [29].

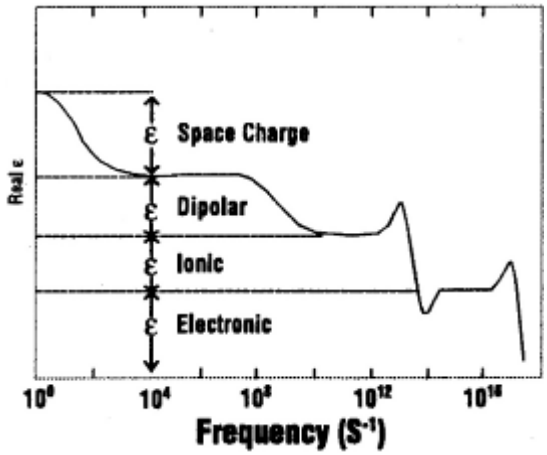

Figure 1.5. Polarization mechanisms and their frequency dependence [36].

"Electronic" refers to the displacement of the electronic cloud relative to the positive core. "Ionic" refers to separation of positive and negative ions with respect to one and other. "Dipolar" involves the alignment of dipoles with the electric field. Finally, "Space Charge" involves the presence of charges impeded by interfaces, or trapped in the material. These polarization mechanisms result in the storage of energy in the dielectric material, resulting in an increase in the capacitance of the device employing them [37].

Capacitance accounts for the different energy storage mechanisms taking place and can be used when calculating the total energy stored. It is possible to derive an expression for the free energy of an electrode by considering that as the capacitor is charged, more and more of the same charges are brought to the electrode plates and are experiencing increasingly repulsive forces. Through Coulomb's law (employing the dielectric constant) it can be seen that

$$F = \frac{Q_1 Q_2}{4\pi\varepsilon_o\varepsilon_r r^2} \quad (1.3)$$

$$G = \frac{Q_1 Q_2}{4\pi\varepsilon_o\varepsilon_r r} \quad (1.4)$$

The force F (Newton) is the repulsive force felt by the (same sign) charges Q1 and Q2 (coulombs), which are separated by distance r. G (Joules) is the Gibbs free energy available from this interaction. As the capacitor is charged, charges of the same sign are added to the same plates which repel one another. This increases the energy of the system. By considering a fraction λ of the total charge q (ultimately reaching λ=1), we can perceive the plates as being charged progressively with λq. Now if we consider an infinitesimal charge δq added to the electrode, we can calculate the incremental increase of free energy in the electrode dG by considering that the potential energy added to the system under a potential V to a charge q is qV, and that V can be found by dividing the amount of charge by the capacitance C.

$$dG = \frac{\lambda q}{C} dq = \lambda V dq \qquad (1.5)$$

$$dq = q d\lambda \qquad (1.6)$$

$$\Delta G = \int_0^1 \frac{\lambda q}{C} \; \mathrm{q d}\lambda \qquad (1.7)$$

$$= \frac{1}{2}\frac{q^2}{C} = \frac{1}{2} C V^2$$

1.3.1.2 Electrochemical Capacitors

Electrochemical capacitors are known as supercapacitors, ultracapacitors, and several other names originating from their military and commercial applications [38, 39]. They consist of electrical contacts (also called current collectors, shown in figure 1.6 as grey metallic plates on the left and right sides of the electrochemical capacitor) upon which active electrode material is placed. The conventional device is symmetric and the two current collector – electrode modules are separated by a membrane. The membrane (shown as a semi-transparent block in the center of the capacitor in figure 1.6) prevents

electrical shorting, but allows ion migration (see figure 1.6). The electrode assembly is immersed in a solution of electrolyte ions. Upon application of a potential, positive ions move towards the negative electrode and negative ions towards the positive electrode, adsorbing on the internal surface of the active material particles (figure 1.6).

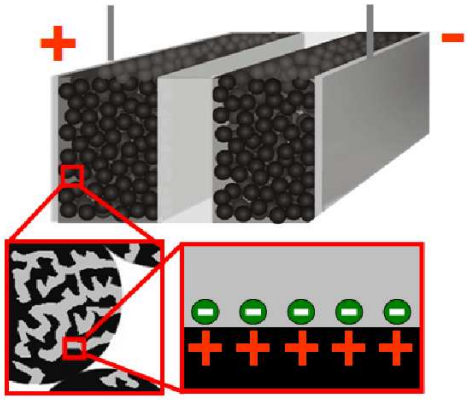

Figure 1.6. Schematic of electrochemical capacitor.

The research initiatives in the electrochemical capacitor field mainly focus on the electrode material, the electrolyte solution, which could be aqueous, organic, and/or ionic liquid, and the separator materials which are often made of cellulose, Teflon, or other polymers [40]. The electrolyte employed is the source of the voltage operation limit of the device, although, unwanted redox reactions of the electrode material may be the cause in some instances. In addition, the conductivity of the electrolyte can have a significant impact on the power performance of the device. Most electrochemical capacitors operate between 1 to 5 volts [41, 42]. Table 1.1 lists some properties of electrolytes used in electrochemical capacitors. Electrochemical capacitors are traditionally categorized into two different types, electrical double layer capacitors (EDLC) and pseudocapacitive capacitors [29].

Table 1.1. Comparison of electrochemical capacitor electrolytes.

Electrolyte System	Pros	Cons
Aqueous	Non-toxic potential, low-cost, high energy density Faradaic reactions	Low operating potential limit < 1 V, highly studied sulfuric acid solution considered unsafe
Organic	Higher operation potential ~2.5 V, high power possible	Lower energy density, flammable, toxic, moisture sensitivity
Ionic Liquid	High operating voltage (up to 5 V), easy handling, reduced flammability	Lowered power due to large ion size, cost

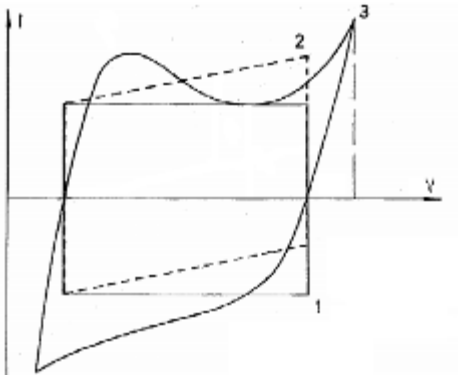

Figure 1.7. Schematic of typical electrochemical capacitor charge/discharge [43] 1 – ideal capacitor, 2 – capacitor with resistance, 3 – non-ideal capacitor.

Figure 1.7 shows the general characteristics observed by electrochemical capacitors in cyclic voltammograms. If the following equations are considered, it can be seen why a rectangular shape is expected from ideal capacitors.

$$C = \frac{dq}{dv} \qquad (1.8)$$

$$I = \frac{dq}{dt} \qquad (1.9)$$

$$C = \frac{Idt}{dv} = \frac{I}{dv/dt} \qquad (1.10)$$

C is the capacitance (F), dq is the differential charge (Coulomb), dv is the differential potential change (V), dt is the differential time change (sec), and I is the current (amps). If the sweep rate (dv/dt) is kept constant, and the capacitance is independent of voltage, then the current response should also remain constant throughout the charging/discharging process, and maintained at the same level for both charge and discharge (see 1 in figure 1.7). If the capacitor is non-ideal and a resistance is present (R), a dependency of the current (I) on potential (V), such as the one seen in ohm's law

$$V = IR \quad (1.11)$$

would account for the linear increase in current as the potential is increased, and decrease when the potential is decreased (see 2 in figure 1.7). The peaks which might appear in a non-ideal capacitor (see 3 in figure 1.7) are due to individual oxidation and reduction peaks, which cause a large deviation in charge (current) exchange. The voltammogram (figure 1.7) often has a mirror image response, which is representative of the high reversibility afforded by electrochemical capacitors. It can also be seen that as the direction of sweep is changed, there should be an immediate reversal of the current direction according to equation 1.10. The mirror-image symmetry is maintained as long as there are no diffusion controlled processes. In the last case different potentials might be required for the anodic and cathodic currents to equalize, and the appropriate diffusion gradients need to be taken into account to predict the shape of the voltammogram [29].

The energy and power densities are two of the most important characteristics of electrochemical capacitors. Energy density is a measure of the amount of charge/energy storage a capacitor is able to hold per mass/volume of electrode material. Power density is a measure of the rate at which stored energy can be delivered. The power density

depends on both the energy density and the time or frequency response of an electrochemical capacitor. The faster the capacitor can be charged/discharged, the higher the power response. Table 1.2 compares standard performance characteristics of solid-state capacitors, electrochemical capacitors, and battery systems.

Table 1.2. Generalized comparison of several energy storage systems [44].

Characteristic	Lead-Acid Battery	Electrochemical Capacitor	Conventional Capacitor
Charge Time	1 to 5 hrs	0.3 to 30 sec	10^{-3} to 10^{-6} sec
Discharge Time	0.3 to 3 hrs	0.3 to 30 sec	10^{-3} to 10^{-6} sec
Energy density (Wh/Kg)	10 to 100	1 to 10	<0.1
Cycle Life	1000	>500000	>500000
Power density (W/Kg)	>100	>1000	>10000

1.3.1.3 Electrical Double Layer Capacitors

The term double layer was coined by Helmholtz in 1857 [7]. When a conductor is placed in a solution of ions, and a potential bias is applied, electric charge resides on one side of the electrode, and ions (of the opposing charge) adsorb on the other side (electrolyte side) of the metal-solution interface (see figure 1.6), thus termed the double layer. This occurs at the opposing electrode, with the sign of the charges reversed [29]. This means that for symmetric, commercial EDLC, two capacitors are operating in series (since there are two electrodes), which results in an approximate halving of the capacitance as compared to a single electrode's capacitance. The solution ions in an ideal EDLC are adsorbed onto the surface and do not involve any chemical reactions (Faradaic reactions), such as those that take place in a battery. This allows for a significantly larger number of charge/discharge cycles (>500,000) compared to popular battery systems (<1000) [30, 45]. Figure 1.8a is a schematic demonstrating the double layer concept as

modeled by Helmholtz. Over time other scientists have modified this model to better explain the distribution of ions relative to the electrode surface, as seen in figure 1.8b [46-50].

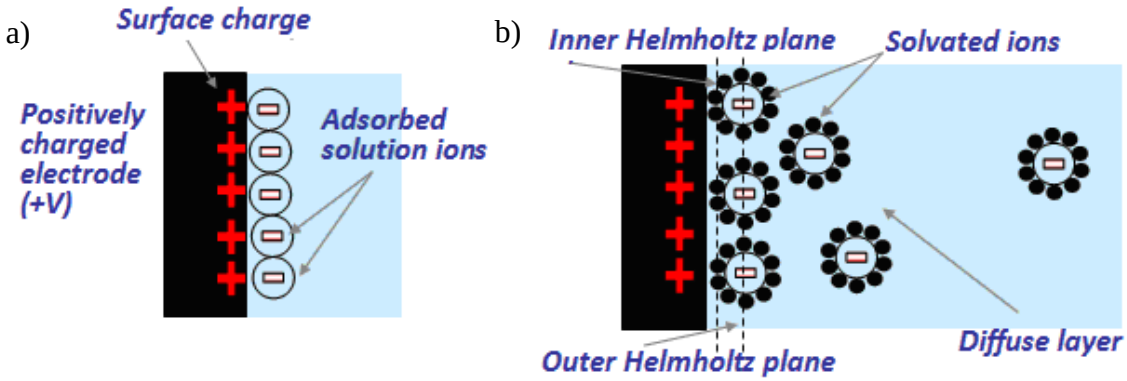

Figure 1.8. (a) Schematic of the model proposed by Helmholtz (b) Schematic of the Guy-Chapman-Stern model [1].

Since the total capacitance largely depends on the surface area, commercial EDLC commonly employ conductive, high-surface area materials, such as porous carbons with well developed porosity, for example activated carbons. These high-area carbons can be made of inexpensive materials such as coconut shells, corn, sugars, and other precursors such as polyacrylonitrile, penolic resin, petroleum coke, anthracite, pitch, and coal [51-58]. The activation process is generally divided into two categories: thermal/physical or chemical. The first step in producing activated carbons in both categories involves carbonization of a precursor (removal of non-carbon species by thermal decomposition in an inert atmosphere). The second step is different for both categories. Thermally produced activated carbons require gasification - development of porosity by partial etching of carbon during annealing with an oxidizing agent, such as CO_2, H_2O, or a mixture of agents at moderate temperatures (below 400 °C). Production of activated carbons by chemical activation generally involves the reaction of the

resulting carbon with a chemical reagent (KOH, $ZnCl_2$, H_3PO_4, H_2SO_4) at elevated temperatures (above 500 °C) [59-61]. The purpose of the second step is to oxidize and remove part of the carbon, thus leaving pores and increasing the BET measured surface-area up to ~ 3000 m^2/g. Activated carbons having surface areas in excess of 2000 m^2 / g have demonstrated capacitance of up to 300 F/g in aqueous electrolytes [1, 42, 62, 63].

The activation process does not result in a tight pore size distribution, which makes it hard to study the effect of pore size on electrochemical performance [64]. Additional carbons being studied as electrode materials for electrochemical capacitors include templated carbons [65-67], carbon nanotubes [68-70], nanodiamonds [70], cloths [71], fibers [71], and other high area carbons, including CDCs [70-73]. Different structures and morpohology provide different performance characteristics. These differences are due to several parameters, including pore sizes, pore shapes, crystal structure, and particle sizes. For instance, a high surface area of activated carbons leads to an increased specific capacitance, but the complex pore structure entailing bottleneck pores may significantly hamper the frequency response of the EDLC based on activated carbons and allow for modest power density characteristics. Carbon onions and multi-walled carbon nanotubes (MWCNT) have lower surface areas than the high capacitance activated carbons, but their open pore structures allow for much faster charging and discharging, leading to better power performance [70]. In addition, the high electrical conductivity of MWCNT, as compared to activated carbons, facilitates further increase in power density [63]. However, the gravimetric capacitance of MWCNT and carbon blacks is generally <50 F/g, while the capacitance of activated carbons and templated carbons can reach 300 F/g [74]. Templated carbons [65-67], with a template-determined porosity may offer a combination of

high capacitance and good frequency response, thus leading to high energy and power density.

Until recently it was believed that the pore size should be on the order of two to three times larger than the size of the solvated ion in order to utilize the surface area of those pores [75, 76]. New evidence reported by Chmiola et al. demonstrated that sub-nanometer pore sizes, which are attainable through templated carbons and CDC, can lead to higher capacitances than those achieved by activated carbons [77-79].

1.3.1.4 Pseudocapacitors

Significantly higher capacitances are attained if use is made of electrochemical reactions such as those obtained by employing metal oxides in aqueous electrolytes. The energy storage mechanism, titled pseudocapacitance, is attributed to fast and highly reversible Faradaic reactions. In reality, reactions are not completely reversible, not necessarily limited to the surface, and result in faster capacitance fading, meaning cyclability is not as high as compared to double layer capacitors employing carbon. These charge transfer reactions, no matter their limitation to the surface and cyclability, store a significantly larger amount of energy in the electrode, as compared to the ion physisorption taking place in double layer capacitors [29, 71]. Unlike the 3D bulk reactions which transpire in battery chemical reactions, it is mostly accepted that the reversible reactions occurring in pseudocapacitors are 2D, and do not entail a phase change [68, 80]. In addition, many of the reactions at the surface of a pseudocapacitor take place over a range of potentials and Faradaic processes, unlike the pronounced individual Faradaic peaks that occur in batteries [29]. This results in the pseudocapacitor voltammogram having a fairly potential independent current response [81]. Figure 1.9 shows the contrast between

batteries and electrochemical capacitors via examination of their voltammograms [29]. Figure 1.9a shows the current-voltage (referenced to the reversible hydrogen electrode) response curve for an electrochemical capacitor (in this case ruthenium oxide), and figure 1.9b shows a typical response curve for a battery (lead/lead chloride). The electrochemical capacitor I-V curve shows a mirror-image response for the different sweep directions (typical of capacitor systems), and an almost immediate reversal of current upon direction change. Although not illustrated in this voltammogram, the capacitance of this metal oxide does not display a strong dependence on voltage sweep rate. In some electrochemical capacitors the presence of micropores and large diffusion distances are expected to result in a sweep rate dependence for the capacitance [82]. The battery, on the other hand, does not show a mirror image voltammogram (figure 1.9b), does not change current direction immediately, and requires significant overvoltages in both sweep directions resulting in a separation of the oxidation and reduction peaks. The semi-rectangle formed by the pseudocapacitor I-V curve (figure 1.9a) is attributed to multiple redox reactions occurring over varying potential ranges that result in a fairly constant charging current at a constant sweep rate [29].

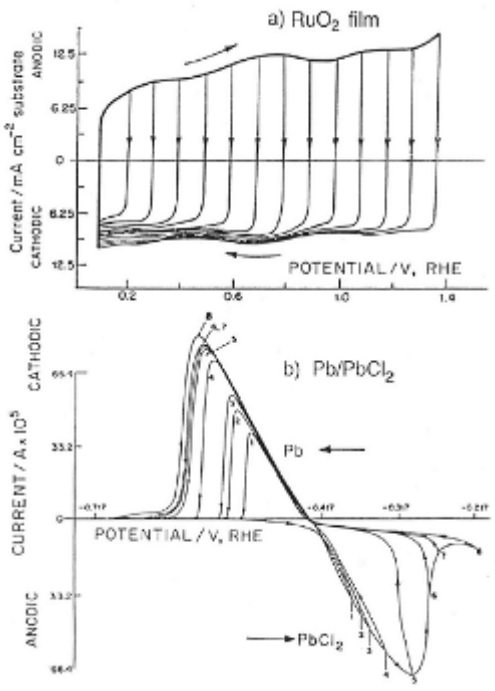

Figure 1.9. Typical cyclic voltammograms of (a) supercapacitors and (b) batteries [29].

The power density of electrochemical capacitors is inversely related to their resistance [83]. The energy density increase provided by metal oxides usually comes with a cost in power density since there is a dependence on slower Faradaic reactions, and metal oxides have low conductivity, which reduces the power density of the electrochemical capacitor as compared to carbon-based electrochemical EDLC. As a result, commercial pseudocapacitors are constructed using the expensive ruthenium oxide, which is fairly conductive for a metal oxide. Thus far most research efforts have focused on ruthenium oxide, iridium oxide, and manganese oxide [84, 85].

Research into the mechanisms involved in metal oxides, such as ruthenium oxide has resulted in some mechanism suggestions (chemisorption reaction described below), but research into the field continues [29, 86]. The suggested chemical reactions for RuO_2, which may be similar to the mechanisms in MnO2 and IrO2 is [80, 86] (forward for charging, backward reaction for discharging).

$$RuOOH \leftrightarrow RuO_2H_{1-\delta} + \delta H^+ + \delta e^- \text{ (anode)}$$
$$RuO_2 + \delta H^+ + \delta e^- \leftrightarrow RuO_{2-\delta}H_{1-\delta} \text{ (cathode)}$$
$$0 \leq \delta \leq 2$$

In aqueous solution, on the cathode side, a proton approaches the surface of the ruthenium oxide electrode, and when a potential is applied, an electron is accepted. Hydrogen is then chemisorbed onto the surface of ruthenium oxide. On the anode side, a lower oxidation state is more energetically favorable to participate at which point a proton can be released, and an electron along with it.

The morphology and crystal structure of the metal oxide in use has been demonstrated to be of extreme importance. There appears to be magnitude differences in energy and power density when ruthenium oxides and manganese oxides are in a hydrated amorphous state, as compared to their non-hydrated crystalline state [81, 87]. In addition, since pseudocapacitance is primarily attributed to surface reactions, it is reasonable to expect that an increase in the surface area of the metal oxide will result in an increase in capacitance, as is seen in the case of hydrated amorphous ruthenium oxide [81]. Although pseudocapacitance is primarily accepted as a surface reaction, there have been reports of diffusion into particles, also known as intercalation. Such reports involved hydrated amorphous ruthenium oxide and hydrated amorphous manganese oxide (in which charging remained reversible and did not entail a phase change), and demonstrated that energy and power density had a dependency on particle size [81, 87].

A group of materials that are of great interest for pseudocapacitors are conducting polymers. The most studied conductive polymers are polythiophene, polypyrrole, and polyaniline [43, 88-92]. The storage mechanism is that of doping and on discharge de-doping

of the polymer backbone. Like some of the metal oxides, cyclability is hampered due to some irreversible side-effects of this mechanism such as structural instability.

1.3.2 Lead-Acid Batteries

A basic LAB consists of a positive and negative electrode divided by a separator in an aqueous solution of sulfuric acid electrolyte. The electrolyte consists of aqueous sulfuric acid solutions of around 29-32 wt.% H_2SO_4 (~1.25-1.28 cc/g-post formation process goes to >1.29 cc/g, ~4-5 mol/L, pH of ~ -1 to -0.75 [93]). In general, the positive active material (PAM) or cathode consists of lead dioxide (PbO_2) and the negative active material (NAM) or anode is a porous sponge lead (Pb). During galvanic discharge these materials are converted to lead sulfate ($PbSO_4$) and during electrolytic charging they are transformed back to lead and lead dioxide. This battery chemistry could not be made possible if the solubility of lead, lead oxides, or lead sulfate were soluble in sulfuric acid to an appreciable degree [94].

Two very important parameters in the description of batteries are the open-circuit voltage (OCV) and the theoretical energy density associated with the Faradaic reactions. In order to calculate the OCV, one must examine the reactions taking place during galvanic discharge as follows:

$$PbO_2 + 4H^+ + SO_4^{2-} + 2e^- \rightarrow PbSO_4 + 2H_2O \qquad (1.12)$$

$$Pb + SO_4^{2-} \rightarrow PbSO_4 + 2e^- \qquad (1.13)$$

Equation 1.12 is taking place at the positive electrode while equation 1.13 is taking place at the negative electrode. The E^0 potentials for the half reactions are +1.6913 V and -0.3588 V vs. NHE at 25 ˚C, respectively [95].

The relationship between Gibbs free energy and the cell potential is as such:

$\Delta G = -nFE^0$

Since the potential of 1.12 is positive and the potential of 1.13 is negative, it is more energetically favorable for equation 1.12 to occur as a reduction of lead dioxide while 1.13 reflects the oxidation of lead. The total potential of the reaction is +2.050 V with a negative change in Gibbs free energy for the total reaction:

$E^0_{cell} = E^0_{cathode} - E^0_{anode} = E^0_{reduction} - E^0_{oxidation} = 1.6913 – (-0.3588) = +2.050$ V

$Pb + PbO_2 + 2H_2SO_4 \rightarrow 2PbSO_4 + 2H_2O \quad E^0=2.050V$

The specific theoretical capacity can be calculated from the equation:

$C_{theoretical} = n^* F / M$

n is the number of moles of electrons per mole of reaction species (in our case 2 e^- per 1 mol of Pb or PbO_2), M is the molecular mass of the electroactive components, and F is Faraday's constant (96,485 C/mol, which is derived from the charge of the electron multiplied by Avogadro's number, or equivalently 26.8 Ah/mol, which is the same amount of charge per mol in F but represented in a form relating current and time). In the case of the lead acid battery, M is approximately Pb (207 g/mol), PbO_2 (239), $2xH_2SO_4$ (196), and n=2, resulting in a theoretical capacity of 83.5 Ah / kg. The theoretical energy density can be calculated using the theoretical capacity for the cell and the experimental operating potential, for a LAB this translates to approximately 167 Wh/kg using an operational OCV of 2 V [14].

During electrolytic charging of the LAB, the following main reactions are observed at the PAM (1.14) and NAM (1.15):

$PbSO_4 + 2H_2O \rightarrow PbO_2 + 4H^+ + SO_4^{2-} + 2e^-$ (1.14)

$PbSO_4 + 2e^- \rightarrow Pb + SO_4^{2-}$ (1.15)

As a result of applying a potential with a window that is larger than 2 V and encompassing the reaction potentials shown in 1.16 and 1.17 it is inevitable to drive the electrolysis reactions at the PAM (1.16) and NAM (1.17):

$H_2O \rightarrow ½\ O_2 + 2H^+ + 2e^-\ E^0 = +1.229\ V$ (1.16)

$2H^+ + 2e^- \rightarrow H_2\ E^0 = 0.0\ V$ (1.17)

Overall Reaction:

$H_2O \rightarrow H2 + ½\ O2\ E^0 = 1.229\ V$ (1.18)

In an effort to combat this loss of water, VRLA batteries were designed to promote the recombination of oxygen at the anode via the following reactions:

$Pb + ½0_2 + H_2S0_4 \rightarrow PbS0_4 + H_2O$

$PbSO_4, + 2H^+ + 2e^- \rightarrow Pb + H_2S0_4$

The oxygen is created at the PAM, travels to the NAM where it forms $PbSO_4$, discharging the active material, and can then be converted back to lead during charging.

1.4 Commercial Device Construction

1.4.1 Supercapacitors

The construction and design of the electrochemical capacitor can cause variations in the electrochemical performance. For instance, inaccessibility to solution, bad interfacial contacts, thermal management and more issues can arise due to incorrect design. Devices have several common designs including spiral wound and monoblocks [96, 97]. The spiral design is very similar to standard battery production methods and the monoblock design entails cells that consist of many positive and negative electrodes in parallel in order to increase the available cross-sectional area. Figure 1.10 and Figure 1.11 illustrate the construction of these two types of electrochemical capacitors.

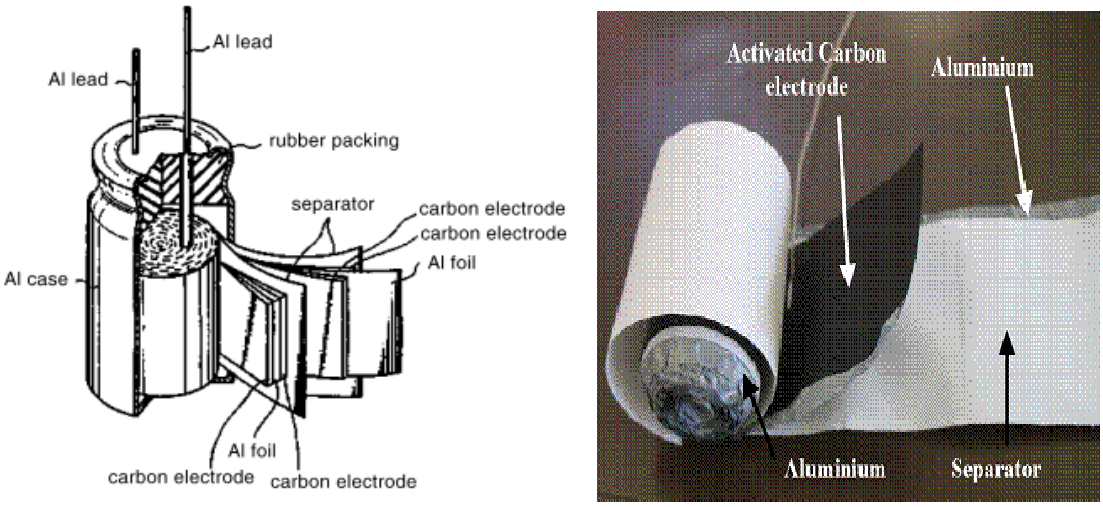

Figure 1.10. Schematic view of a Panasonic EDLC [97, 98].

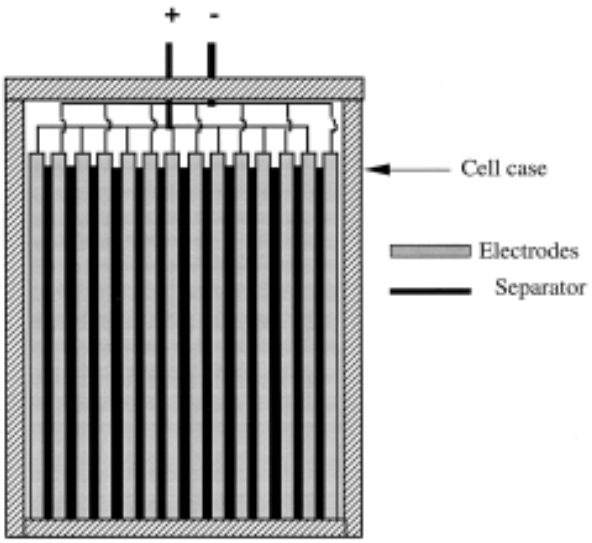

Figure 1.11. Cross-section of monoblock EDLC [96].

In addition to these designs there is also an all-solid design which can enhance the safety providing safer handling and reduction in flammability [99, 100].

1.4.2 Lead-Acid Batteries

The construction and design of LABs, as in the case of ECs, is very important as it has an effect on performance. When designing the cell, it is important to use low cost materials that are robust enough to handle the needs of the application. A very common

application of LABs is for SLI in vehicles. In this case the LAB must withstand the constant vibrations and changes in temperature in addition to the necessary electrochemical performance needs. LABs often come in either one of two constructions, spiral or prismatic type as shown in figures 1.12 and 1.13. That said, there is another less successful design known as the bipolar construction [101]. The case of the LAB is often made of polypropylene with strengthening additives [101]. The case is meant to be resistant to electrolyte leakage, temperature resistant, structurally resilient, and chemically inert to the electrolyte. Each cell produces approximately 2.1 V and, in order to bolster the voltage, cells are connected in series via lead castings and in parallel for increased power. The battery can be fitted with a valve to release pressure in case of excessive gas pressure buildup, hence the name valve-regulated lead-acid battery. Previously most cells were not as impermeable and would require refilling. In the prismatic case the cells can be placed in pouches to contain the material and act as separators while being submerged in an excess of electrolyte (figure 1.13), or they can be gelled via silica, or contained in an AGM separator without excess electrolyte. In the spiral battery case, the cells are likely in individual cavities as shown in figure 1.12 and AGM used as separator, though other constructions are also possible for both variants. These variations are a result of the different possible configurations available to battery designers. Parameters to vary include, spiral, prismatic, gelled, flooded, or AGM, separator types – AGM, pouch, physical cell separation (figure 1.12), sealed, unsealed, and so many more.

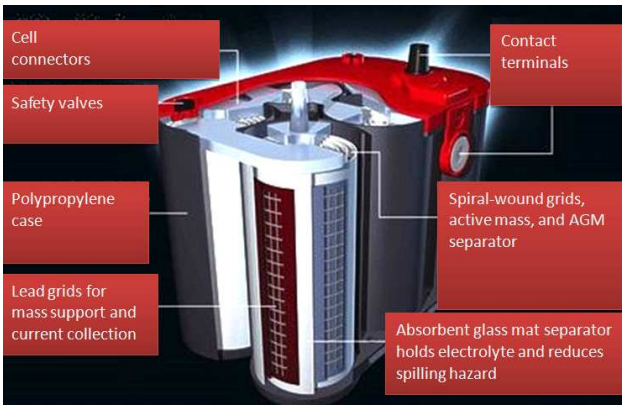

Figure 1.12. LAB Spiral cut-away [102].

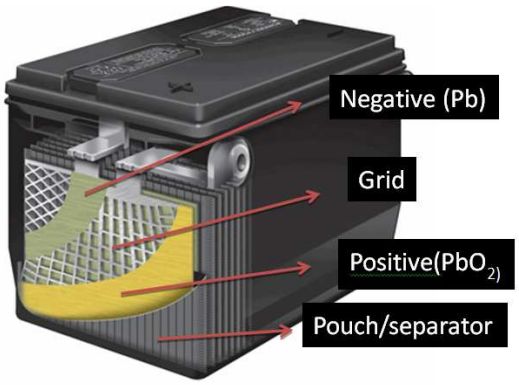

Figure 1.13. LAB block cut-away [103].

1.5 Zeolite-Templated Carbons

In the past 5-10 years there has been a growing interest in templated carbons for a variety of important applications, such as fuel cells [104-108] , ECs [109-111, 112-116], hydrogen storage [117-119,64] , and catalysis [104,106-108]. The interest in templated carbons does not lie only in their good performance in such applications, but also in their ability to simplify a system in order to facilitate the study of various mechanisms. In commercial ECs the carbon utilized is a by-product of the anoxic pyrolysis and activation of organic materials like corn husks, coconut shells, and other cheap materials [120], but the resulting pore structure is very complex, containing a broad pore size distribution and is not conducive

to the researcher's attempt to understand the mechanisms underpinning the electroadsorption of the ions involved in energy storage. Templated carbons allow for a very tight pore size distribution and control that can overcome this issue. Prior studies suggested that an increase in capacitance occurs when pores are small enough (~ <1nm) to deform the solvation shell. This fact may never have been demonstrated were it not for the carbon having a uniform pore structure [121]. Previously studied zeolite Na-Y templated carbons have shown a dual pore size distribution with pores slightly smaller and slightly larger than 1 nm, allowing for high specific capacitance and high ion mobility, resulting in high energy and power density [116]. The uniform pore structure conferred, for example, by a Na-Y zeolite, makes it much easier to study the ion-surface interaction taking place in ECs. The ability to control the pore size of a templated carbon to a high degree makes templated carbons an important tool from both a scientific and engineering perspective and for the study of various energy storage systems incorporating them, such as ECs. Surprisingly, the study of ZTCs in ECs have been fairly limited [109, 116, 122-128] and their application have never been studied in LAB.

1.6 EDLC Characterization Methods

Important performance qualities of electrochemical capacitors include specific capacitance, energy density, and power density. These characteristics are modulated by various parameters including the materials used for the electrode, the electrolyte, interfacial resistances, the separator membrane, and cell design. This study is focused on the effect of parameters varied during synthesis of the active electrode material. The study will attempt to explain correlations between properties like surface area, pore morphology, size and distribution, and electrochemical performance. In order to

characterize this performance, electrochemical testing including charge-discharge (Galvanostatic), cyclic voltammetry and impedance spectroscopy were employed and techniques like x-ray diffraction, scanning electron microscopy, and gas sorption techniques were used to examine the physical properties of the material.

1.6.1 Galvanostatic Test

Galvanostatic testing applies a constant current to the electrochemical capacitor using a galvanostat and the resulting voltage change with time is measured. This results in charging of the capacitor up to a pre-set voltage. The capacitor is then discharged and the voltage drop with time is measured. A typical charge-discharge (C-D) graph is illustrated in figure 1.14.

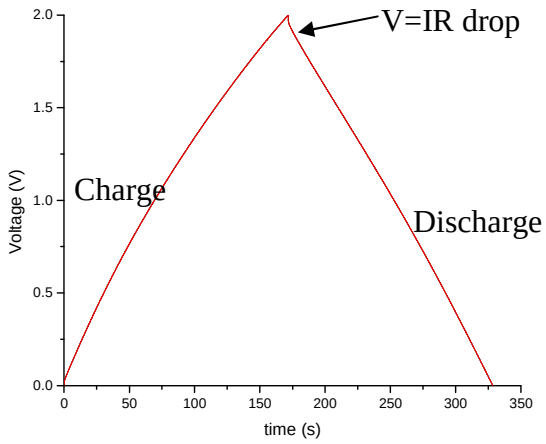

Figure 1.14. Galvanostatic (C-D) graph of CA29 at 0.8 A/g resulting in 113 F/g.

In figure 1.14 the device has a fairly low IR (potential) drop due to its low internal resistance or, as it is commonly termed, equivalent internal series resistance (ESR). This technique allows for a determination of the equivalent internal series resistance by quantifying the drop upon discharge (V=I*ESR). The ESR has several contributions to it including the electrical resistance of the carbon electrodes, the interfacial resistance

between the current collectors (contacts) and active electrode mass, and ionic resistance of the electrolyte. The C-D test provides information on the (specific) capacitance of the device (F/g), energy density (Wh/kg), power density (W/kg), ESR (Ohm), and the affect of current density on these characteristics. Using equation 1.10 to find the capacitance of the total device, then dividing it by two since there are two electrodes working in series (and assuming they are the same) and then normalizing it by the mass of one electrode, one can calculate the gravimetric capacitance. The energy density in Ws/g is obtained by using equation 1.7 and normalizing it to the mass. It is then multiplied by 1000 (for kg) and divided by 3600 (1Wh=3600J) to get Wh/kg. To get the power (W/kg) the value in Ws/g is multiplied by 1000 and divided by the discharge time in seconds. Figure 1.15 is a Ragone plot showing power vs. energy density. As the charge-discharge happens at higher rates the power increases, but the energy density is reduced due to the inability of the ions to respond quickly enough to form the double layer and/or allow for the necessary Faradaic reactions to take place.

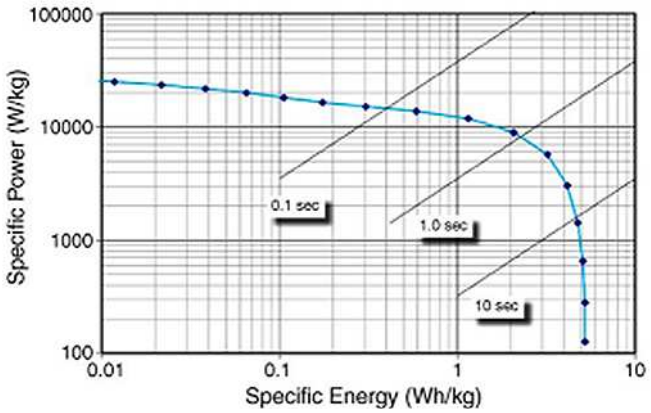

Figure 1.15. Ragone plot of a commercial 350 F capacitor (BCAP0350 Maxwell Technologies) [129].

1.6.2 Cyclic Voltammetry

Cyclic voltammetry (CV) is an electrochemical characterization technique involving the current response of a device with respect to a voltage change. This measurement applies a constant sweep rate (dv/dt) and monitors the current response of the two-electrode device. The sweep was done at varying rates to see the effect on capacitance and at various potential ranges, wherein the electrolyte remains stable. The information gathered from this characterization technique includes the (specific) capacitance (via equation 1.10 using the average current calculated by integrating the area and diving by the voltage range), effect of sweep rate on capacitance, and possible information on the resistance/response of the device based on the shape of the cyclic voltammogram. For instance, as seen in figure 1.9, the ideal shape of a capacitor (rectangular) is often not seen due to possible Faradaic reactions and the linear increase in current is due to the device's resistance. In this investigation the use of two-electrode cyclic voltammetry and mostly double-layer capacitance associated with carbon results in fairly symmetric voltammograms, excluding the current increase with increasing potential.

1.6.3 Electrochemical Impedance Spectroscopy

Electrochemical impedance spectroscopy (EIS) evaluates the electrochemical response of the electrochemical capacitor to an AC signal at various frequency rates. Generally, the response is plotted in the form of a Nyquist plot as illustrated in Figure 1.16. From the imaginary part of the impedance the capacitance vs. frequency response can be extracted using the following equation

$$C' = -\frac{1}{2\pi f Z''}$$

The ESR of the device can be found by looking at the impedance value at the point at which the graph intersects the x-axis (see figure 1.16).

It should be noted that information regarding the interfacial contact resistance between the contact and electrode can be quantified by using the diameter of the semi circle formed at high frequencies (not seen in figure 1.16, but in the data section).

Also, when looking at the imaginary component, or dissipative component of the capacitance (C”) via the equation below, the maximum corresponds to a transition frequency between the capacitive (low frequency) and purely resistive (high frequency) regimes of operation [126]. The inverse of this transition frequency corresponds to a time constant τ_o, which provides an approximate measure of the appropriate frequency for utilization of the material and its performance relative to other materials.

$$C'' = \frac{Z'(\omega)}{\omega |Z(\omega)|^2}$$

$$f_{trans} = f_{C''\max}$$

$$\tau_0 = \frac{1}{f_{trans}}$$

At frequencies between 1 and 100 Hz the graph has a 45° slope and is associated with the ions infiltrating the porous carbon structure. It is termed the distributed resistance regime. At low frequencies The graph attains an almost vertical shape and behaves much like an ideal resistor and capacitor in series and is no longer frequency dependent like it is at higher frequencies [129].

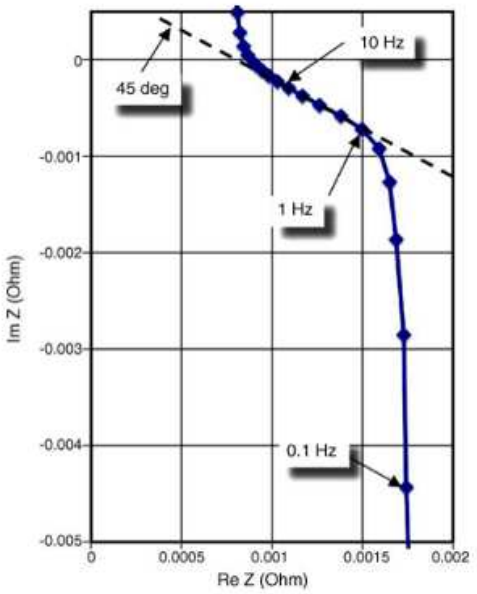

Figure 1.16. Nyquist plot of the impedance behavior of a 350 F capacitor (BCAP0350 Maxwell Technologies) [129].

1.7 Lead-acid Battery Characterization Methods

Important performance qualities of LABs include their capacity vs. charge and discharge rate, power performance, charge acceptance characteristics, temperature effects, and cycle life. These characteristics are modulated by various parameters including the materials used for the electrode, the electrolyte, compression, the separator membrane, and cell design. The electrochemical tests have a lot in common as they are performed by either controlling the voltage of the cell and monitoring the corresponding current (power, not shown, figure 1.17, static-charge acceptance) or controlling the current and monitoring the voltage (capacity, not shown, figure 1.18, cycle life).

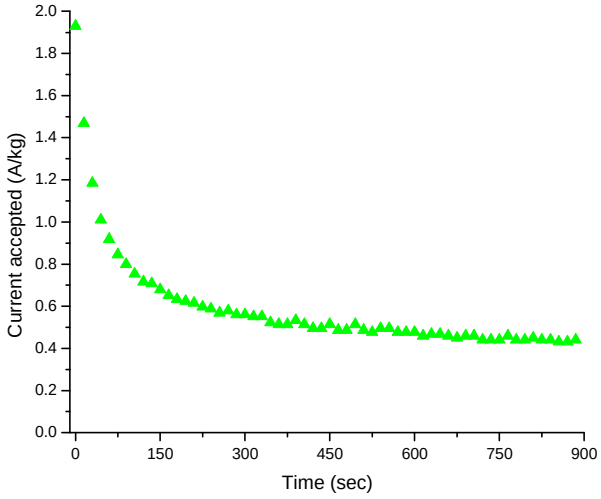

Figure 1.17. Static charge acceptance test of a two electrode LAB, current monitoring at a constant voltage.

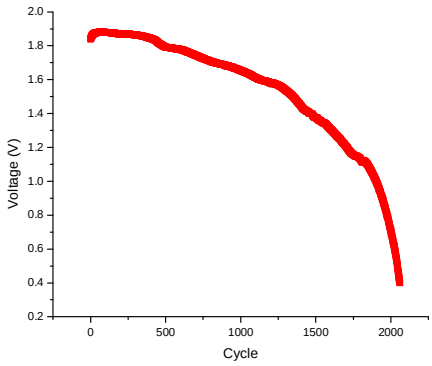

Figure 1.18. Cycle life testing of a two-electrode LAB. Constant current charge and discharge with respective monitoring of the potential.

The work in this study is focused on examining the effect of a conductive-hydrophilic additive on the capacity, power, charge acceptance, and cycle life of LABs. The study aims to examine the electrochemical characteristics of a composite particle as compared to standard LAB materials. In order to characterize this performance, a variety of electrochemical testing methods employing control of current and voltage were utilized and are described in the sections below and techniques such as SEM, TEM, and gas sorption studies were used to examine the physical properties of the material.

1.8 Material Characterization Methods

1.8.1. Gas Sorption

Surface area and pore sizes of EDLC electrode materials are critical parameters for EDLC operation. They are generally examined using nitrogen, argon and/or carbon dioxide gas sorption studies. In the studies discussed in this thesis physical adsorption and desorption phenomena are of main concern. Physical adsorption of gas onto solids increases with decreasing temperatures and increasing pressures. In order to allow for an investigation using physical adsorption and desorption, the first step in our studies involves removing residual moisture from our samples by flowing an inert gas like nitrogen or applying a vacuum while keep the materials at elevated temperatures. Once this procedure is complete the mass of the samples is determined and the sorption studies can begin. During the measurement, the sample is maintained at a constant temperature cooled in liquid N_2 (77 K) when using N_2 gas, or a water-ice bath (273 K) when using CO_2, or liquid Argon (87 K) when using Ar gas, while the adsorptive gas is pumped at incremental pressures into the tube containing the sample under investigation. An isotherm is thus collected, which is a measure of the volume of gas (273 K, 760 Torr - STP) adsorbed at a constant temperature as a function of relative pressure (absolute pressure normalized to the condensation pressure). The isotherm can then be used to derive information regarding the available surface area, pore volume, and pore size distribution of the material, amongst other characteristics, using a variety of models, e.g. BET, DFT, t-plot, and various others. Figure 1.19 shows an isotherm collected using Argon gas as the adsorptive and liquid argon to maintain a constant temperature while dosing a zeolite-carbon composite material.

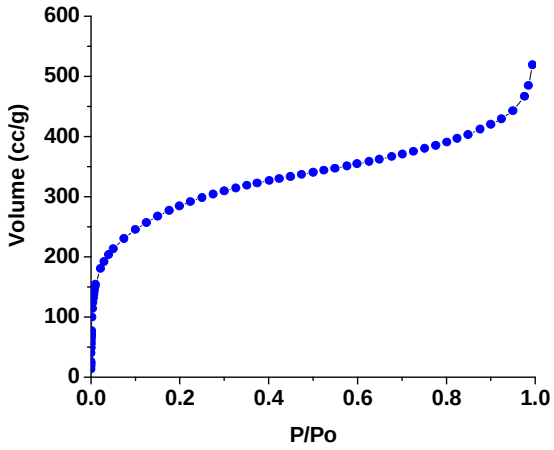

Figure 1.19. Argon sorption (adsorption branch only) isotherm collected at 87 K on a zeolite-carbon composite.

The theory that laid the foundation for the calculations that permitted the surface area measurements and pore structure evaluation comes from the work of Irving Langmuir. His theory assumes that the surface is homogeneous, that there is a monolayer adsorption on the surface of the studied material, and that the adsorbed molecules do not interact. The theory was further developed by Stephen Brunauer, Paul Hugh Emmet and Edward Teller (BET). Their theory applied Langmuir theory to multiple layers of adsorption and assumed that Langmuir's theory can be applied to each layer and that each layer does not interact with the other [130]. The BET equation in its standard form is derived by equating the rate of condensation of gas molecules to an already existing layer to the rate of evaporation from that layer and integrating over an infinite number of layers resulting in the following expression:

$$V_a = \frac{V_m C P}{(P_0 - P)\left[1 + \left(C - 1\right)\frac{P}{P_0}\right]} \qquad (1.19)$$

Or, rearranged

$$\frac{P}{V_a(P_0 - P)} = \frac{1}{V_m C} + \frac{C - 1}{V_m C}\left(\frac{P}{P_0}\right) \qquad (1.20)$$

The expression can be used to find V_m, the volume of the gas necessary to form a monolayer. In equation 1.19, P is the equilibrium pressure, P_0 the saturation pressure, V_a the volume of gas adsorbed at P, and C is a constant. P/P_0 is the relative pressure of adsorptive. C is a constant that is related to the heats of adsorption (q_{ads}) of the first layer and heat of liquefaction (q_{liq}) of the adsorptive (R gas constant, T absolute temp) [131]:

$$C \propto \frac{q_{ads} - q_{liq}}{RT} \qquad (1.21)$$

Equation 1.20 can be plotted as $\frac{P}{V_a(P_0-P)}$ vs. $\frac{P}{P_0}$ yielding a straight line providing C and V_m. Using the volume of the adsorbed monolayer and mean area per molecule (16.2 $Å^2$ for nitrogen and 14.2 $Å^2$ for argon at 77K and 87K, respectively), the surface area can then be derived.

In order to examine the pore size distribution of the samples, various models may be employed. One method of modeling is known as density functional theory, which relies on molecular-based statistical thermodynamic theory. The use of DFT for pore size analysis has been popularized over the past two to three decades by the proliferation of instruments providing turn-key operation along with improved computational power in desktop computers. The benefit over various other models developed for pore size analysis is that DFT can provide one model that can apply over the range from microporous to macroporous unlike other models that are generally limited to the various regimes and required less computation time than other models. The downside is that it is often more involved than the small number of parameters associated with other models and is often tailored towards interactions with specific materials (carbon and zeolite are popular materials for which DFT models have been developed)[131]. DFT uses modern physical chemistry to calculate the distribution of atoms within the pores by assuming the

forces/interaction energies (e.g. Lennard-Jones potential) between atoms and the adoption the lowest free energy configuration at equilibrium. The DFT model is used to generate model isotherms for a variety of pore sizes offline and then post measurements of the materials under investigation. A deconvolution method is used to apply the model isotherms to the experimental isotherm for estimation of the pore size distribution [131].

1.8.2 Electron Microscopy

Electron microscopy was developed in the 1930's in order to exceed the resolution afforded by optical microscopy, both SEM and TEM prototypes were built in the 30's [132]. Electron microscopy has developed into a set of devices dedicated to various tasks, amongst them SEM and TEM that can provide information regarding structure and chemical composition [132]. Scanning electron microscopy (SEM) images the surface by scanning it with a high-energy beam of electrons. The beam interacts with the surface atoms (to some small depth of up to a few microns) and produces signals that contain information about topography, composition, and other possible information such as structure. The signals emitted from the surface include secondary electrons, back scattered electrons, characteristic X-rays, and other various types of radiation. The common method of characterizing the topography is via the secondary electron imaging with up to 1 to 5 nm resolution. Typically the electron beam is created by heating a filament and then accelerating the electrons via a potential. The beam's energy is between 40 keV and a few hundred keV and is focused by one or two condenser lenses to a spot between 0.5 and 5 nm in diameter. As the beam passes through the SEM column (figure 1.20) it is collimated with various coils or deflector plates and is then rasterized across the surface of the sample to form an image.

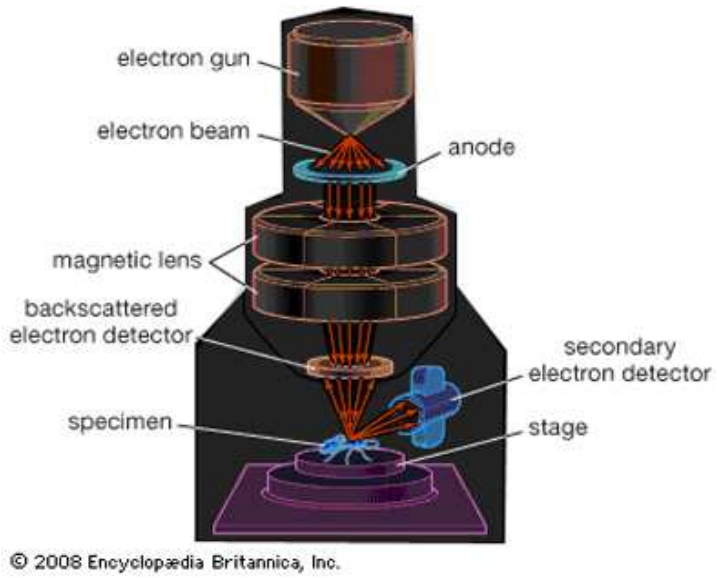

Figure 1.20. Schematic of scanning electron microscope [133].

TEM is an extremely popular tool for the microstructural characterization of materials. Generally, TEM is used for imaging of thin, electron-transparent samples and allows for spatial resolution down to the sub-Angstrom level [132]. It allows for examination of diffraction patterns, like those afford by X-ray diffraction, which provide more quantitative results, but cannot be focused as easily as an electron beam onto desired features. TEM provides a means to focus on microscopic features to examine defects through diffraction contrast and can even allow its user to observe the columns of atoms comprising the materials under investigation [134]. The basic construct of a TEM utilizing a fluorescent screen for observation of the electron beam post interaction with the sample is shown in figure 1.21A. In figure 1.21B the basic beam path is displayed. In essence once the beam has been constrained to a desired dimension via the various apertures, the incident wave impinges upon the thin sample. The interaction is dominated by an elastic scattering process resulting in a signal that is the squared amplitude of the Fourier transform of the scattering potential V(r). The objective lenses then act as Fourier

transform operators allowing for formation of a direct image of the scattering potential as a 2D projection of the scattering center [132].

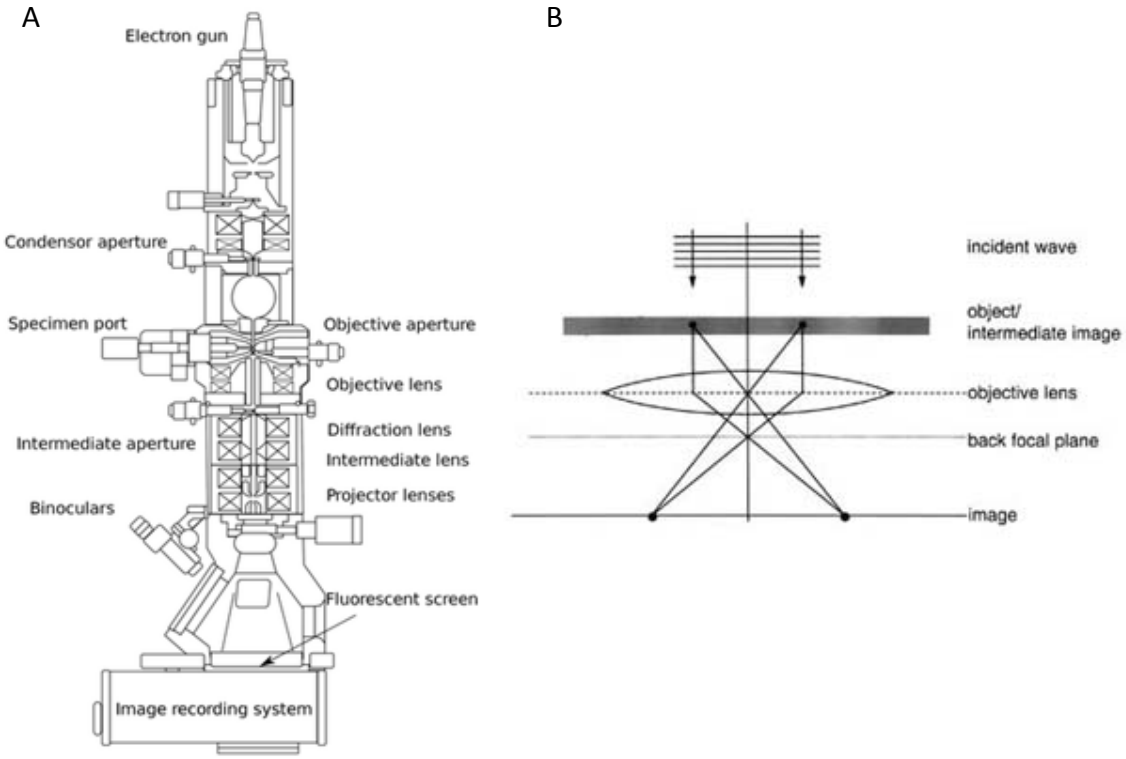

Figure 1.21. A) Outline of the internal components of a basic TEM system [135] and B)simplified schematic of the electron beam in the TEM [132].

CHAPTER 2
MATERIALS AND EXPERIMENTAL METHODS

2.1 Materials

2.1.1 Zeolite-Templated Carbon and Zeolite-Carbon Composite Formation

Zeolite NaY powder (product number: CBV100, Zeolyst International, Delfzijl, Netherlands) was placed in a 10 cm long quartz boat and heated inside a 3 cm in diameter horizontal quartz tube, which was placed in a Barnstead Thermolyne 21100 tube furnace, to the desired temperature under Ar flow at low pressures (<10 Torr). At the desired temperature, the Ar flow was halted and acetylene gas was then allowed to flow over the zeolite powder at a flow rate of 100 sccm at low pressures (<10 Torr) for the desired amount of time. After deposition, the acetylene flow was stopped and the carbon-coated zeolite powder was allowed to cool below 300 °C before retrieval under Ar flow. Selected samples were post-annealed prior to cooling down at either 800 °C or 900 °C for one hour and then cooled. The ZTC samples included samples synthesized at 700 ˚C for 4 hours, with some samples annealing afterwards at 800 ˚C or 900 ˚C for one hour. In the ZCC case, the samples were synthesized at 800 ˚C for 30 min.

For the ZTC preparation, after the carbon deposition, the carbon-coated zeolite powder was submerged in an HF solution (50%) for at least one night, after which the powder was rinsed and filtered. The sample was then placed for additional cleaning in H_2SO_4 (98%) for at least one night, followed by water washing and filtering. Finally, the powder was washed and filtered repeatedly to remove the remaining acid. In the case of the zeolite-carbon composite (ZCC) for the LAB application, the carbon-coated zeolite was placed in a plastic beaker with saturated sodium hydroxide solution. This solution

was put on a hot plate set at approximately 60℃ and stirred occasionally with a glass rod for approximately one hour. The solution was allowed to cool and sit while etching for several days. This solution was filtered and rinsed repeatedly. Then a concentrated solution of hydrochloric acid was used in a similar fashion to the sodium hydroxide and filtered and rinsed repeatedly. All porous carbon samples that were produced were subsequently placed under vacuum to dry. The dry ZCC was ball milled for approximately one hour and a sieve was used to separate the powder from the milling media. One sample termed functionalized zeolite-carbon composite (FZCC) was further treated by heating in sulfuric acid (1.265 cc/g, trace metal grade) for 24 hours at approximately 71 ˚C and then washed, filtered, and dried in a convection furnace at approximately 80 ˚C overnight.

2.1.2 Electrode Preparation and Device Assembly

EDLC ZTC powders were suspended in ethanol and mixed with polytetrafluoroethylene (PTFE) (60 wt. % water suspension, Sigma Aldrich, USA) binder to form a slurry consisting of carbon (95% wt) and PTFE (5% wt.). After drying overnight at ~80 °C under vacuum the electrodes were calendared to a thickness of ~ 0.2 mm using a commercial rolling mill and left to dry in a vacuum oven at ~80 °C for several hours prior to device assembling.

The EDLCs were assembled in a symmetrical two-electrode configuration using 2016 stainless steel coin cells. Al foil was roughened using 600 grit SiC sandpaper, coated by a thin layer (~10 µm) of conductive paint (Superior Graphite), and used as a current collector. The conductive paint was used to reduce the interfacial resistance between the electrode and the current collector. A GORE^{TM} membrane (W.L. Gore and

Associates, US) of ~25 µm in thickness and ~60% porosity was used as the separator for the EDLC devices. Electrolytes were prepared in inert atmosphere gloveboxes, filled with Ar and containing less than 1 ppm of H_2O. For the preparation of the novel electrolyte, AN and MF (Sigma Aldrich, USA) were mixed in a 1:1 volume ratio, and SBP-BF_4 (0.25 M) (Japan Carlit Co., Ltd.) (except for the mesoporous activated carbon sample that employed 0.5 M SBP-BF_4 and the ZTC sample using TEA-BF_4 in AN:MF was 0.5 M) was dissolved in the blend with magnetic stirring at room temperature.

The LAB electrodes were made by mixing lead oxide (PbO) with proprietary binder fibers, expander materials, water, and sulfuric acid for the control electrode (PAM and NAM). The ZCC was added to target the ~1 and ~2 wt. % NAM electrodes (referenced as ZCC and 2X ZCC). The electrode materials were dry mixed, then water was added, followed by drop-wise addition of the sulfuric acid, and water if necessary for flow. The electrode materials were pasted with a spatula onto a lead (Pb, with various additives) grid that was cast using a furnace and a mold. The electrodes were treated with a proprietary humidity and heating regime. Then the electrodes had Pb leads soldered onto them for contact purposes. The electrodes were assembled into a cell by using 3 cathode controls and 2 anode electrodes (control, 1 wt. % ZCC, 1 wt. % FZCC, and 2 wt. % ZCC). Each anode was wrapped in AGM separator and two PP sheets were used as spacers to fill the PP container and electrodes assembly. An aqueous sulfuric acid solution (1.255 g/cc) was added to submerge the cells in electrolyte and then plugs were used to fill any cavities in the container along with glue applied to the seams via a glue gun. The assembly process is portrayed in figure 2.1.

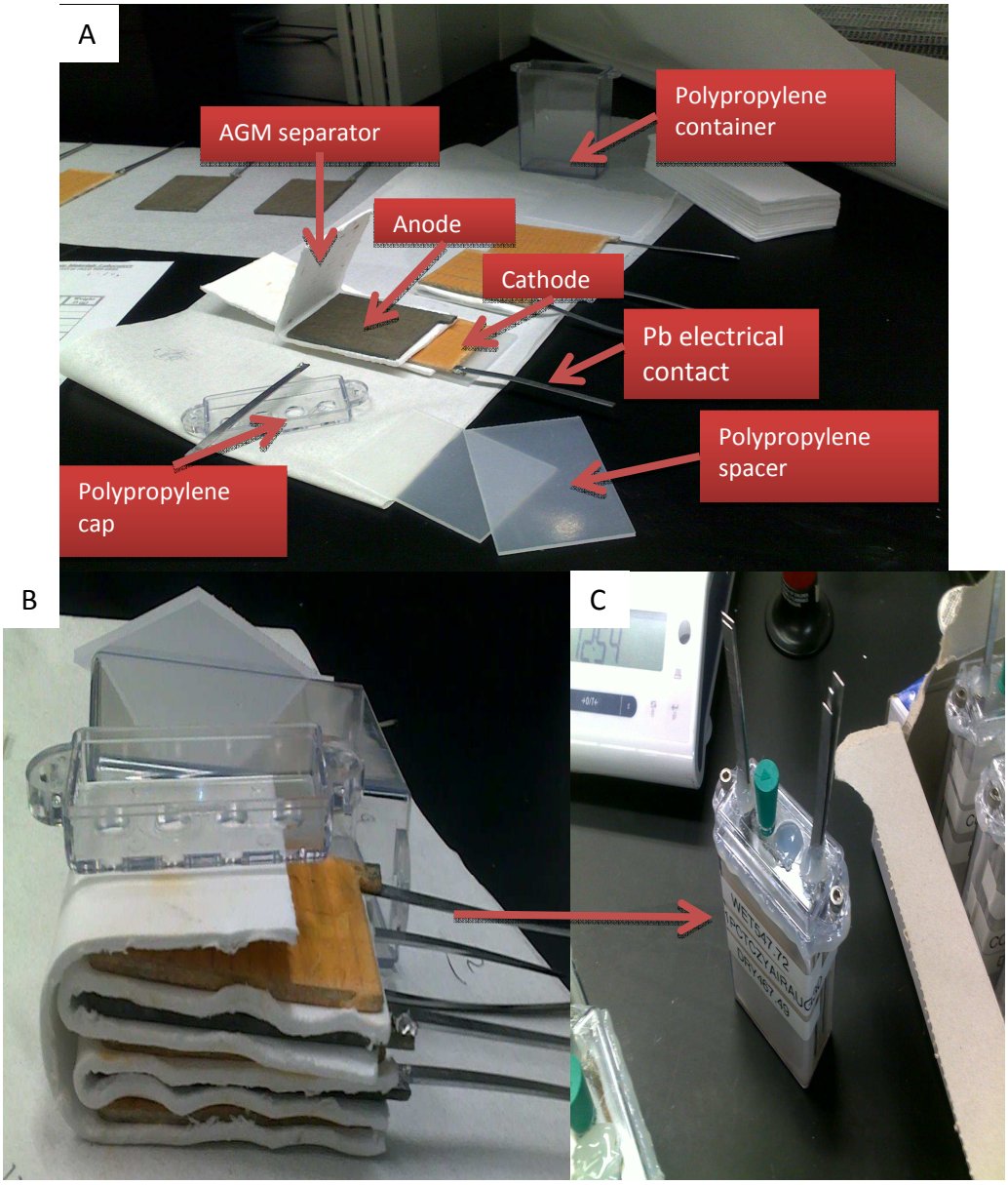

Figure 2.1. Cell assemblies for LAB electrochemical testing. A) Various components. B) Electrode and AGM assembly, PP container and top. C) Complete cell.

2.2 Electrochemical Measurements

2.2.1 EDLC

The cyclic voltammetry (CV) tests were carried out using a Solartron 1287 Electrochemical Interface in the voltage range between -2 to + 2 V. The gravimetric capacitance, C (F g^{-1}), was calculated according to:

$$C = \frac{2I}{(dV/dt)\cdot m} \tag{2.1}$$

where I is the current (A), dV/dt - the slope of the discharge curve (V s^{-1}), and m – the average mass of the carbon electrode (g). Potentiostatic electrochemical impedance spectroscopy studies were carried out using a Zahner IM6 electrochemical workstation (Zahner-Elektrik, Germany) in the frequency range of 1 mHz to 100 kHz with a 10 mV AC amplitude. The specific capacitance was calculated according to:

$$C = \frac{2\cdot\left|\mathrm{Im}(Z)\right|}{2\pi f\cdot\left[(\mathrm{Im}(Z))^2+(\mathrm{Re}(Z))^2\right]m} \tag{2.2}$$

where f is the operating frequency (Hz), Im(Z) and Re(Z) are the imaginary and real parts of the total device impedance, and m is the mass of carbon in each electrode. The equation was expanded to allow for the mass magnitude to modify the contribution of each electrode.

2.2.2 Lead-acid Battery

In order to study the effect of hydrophilic and conductive ZCC in the NAM of the LAB several variations of the charge-discharge tests were conducted on the LAB cells. These tests were written so as to examine the capacity vs. rate characteristics, ability to accept charge, power, and cycle life of the cells. In order to do examine these characteristics several systems were used for testing based on availability and needs of the tests (e.g. current limitations).

2.2.2.1 Capacity Test

In order to examine the energy density of the LAB a capacity test is performed. This entails discharging the battery at a set current rate and taking the integral of the current vs. time curve to obtain the capacity (Amps*h=charge/time*time=charge) of the LAB under different current rates (C-rates) until a set cut-off voltage. The C-rate is assumed to be the current that would be needed as the discharge current to reach the cut-off voltage in one hour (C/20 means discharge over approximately 20 hours). Discharge rates of C/20, C/8, C, 2C and 4C are presented below.

2.2.2.2 Static-Charge Acceptance Test

The static-charge acceptance test is an industry developed test performed in order to examine the ability of the cell to accept charge at 0 ˚F (-18 ˚C). The cell is discharged to 80% state-of-charge (SOC) at a C/20 rate. The cell is then brought down to -18 ˚C (0 ˚F) and equalized for 2 hours. A charging voltage of 2.4 V is applied, and the current response is measured for 15 minutes to examine its ability to accept charge at this state.

2.2.2.3 Power Test

The power test is similar to the static-charge acceptance test in that it monitors the current response of an electrochemical cell to an applied potential, however, there are several differences. The power test was done at room temperature and at 80% and 60% SOC. The cell was first charged to 100% SOC and then charged and discharged at ten second bursts is measured with a 2.67 V applied. Then the cell was discharged at C/20 rate to the next state of charge and the charge and discharge bursts were repeated.

2.2.2.4 Cycle Life Test

The cycle life test was done in the format of an HRPSOC cycling. The cell was discharged to 60% SOC at a rate of C/20. Then the cells were subjected to cycling according to the following schedule: charge 2C rate for 60s, rest for 10 s, discharge at 2C rate for 60 s, rest for 10 s, then discharge and charge back to 60% SOC. The cell was considered to be at the end of its life when it reached the cut-off voltage of 0.4 V. The current control and potential measurement was accomplished via a Maccor potentiostat.

2.5 Gas Sorption

For the ZTC the N_2 adsorption isotherms were measured at 77 K using a Micromeritics ASAP 2420 instrument and ultra high purity N_2 gas (Airgas, USA). Prior to the adsorption measurements the samples were outgassed for 12 hours at 620 K under high vacuum. NLDFT models were used for pore size distribution analysis and NLDFT SSA derivation along with the BET method for calculation of the SSA. In the case of the NAM incorporating the zeolite and ZCC composites, the BET SSA was measured using a Micromeritics TriStar II 3020 via ultra high purity N_2 gas and liquid N_2 after degassing at 100 °C for 30 minutes. For the measurement of the surface area of zeolite, and ZCC a Qunatachrome Autosorb iQ station 1 with ASiQwin software was used with ultra high purity Ar gas and liquid Ar (Matheson Tri-Gas, USA), after outgassing at 70 °C 1 hour, 120 °C 1 hour, 200 °C 1 hour, and then 12 hours at 350 °C (zeolite) or 300 °C (all other samples) and NLDFT models for pore size distribution along with BET for SSA.

2.6 Electron Microscopy

For the ZTC studies, a LEO 1530 SEM microscope (LEO, Osaka, Japan, now Nano Technology Systems Division of Carl Zeiss SMT, MA, USA) was used with an in-lens secondary electron detector, with most of the studies utilizing an accelerating voltage of 5 kV and a working distance of 3 mm. TEM observations were carried out using a Philips CM200UT microscope that has 1.8 Å point- to- point resolution and operates at 200 kV. For the ZCC studies, a Jeol 100CX II TEM (JEOL Ltd, Tokyo, Japan) was used at 100 kV, and a Zeiss EVO MA 10 SEM using a secondary electron detector, at ~20 kV and a 6 mm working distance.

CHAPTER 3

IN-SITU STUDIES OF ION TRANSPORT IN MICROPOROUS SUPERCAPACITOR ELECTRODES AT ULTRA-LOW TEMPERATURES

3.1 Introduction

The need to develop efficient, rechargeable high-power energy storage devices that can operate at temperatures significantly lower than those currently attainable, stems from the demands of industrial activities in low-temperature regions [136], astronomical observatories necessitating operations in polar regions [137], the development of electrical aerial vehicles, and the increasing application of energy storage devices in space and high altitude aircraft [138,137]. High-power, rechargeable, energy storage devices are needed for use in wind-turbine pitch control, in optimizing intermittent solar power utilization, as power sources for communication devices, sensors and other electronic devices, for cold-cranking gasoline and diesel engines, and for regenerative braking and acceleration in hybrid electric vehicles (HEVs). In unmanned and manned aerial vehicles high-power energy storage devices are needed for manipulating wing pitch and other peak power applications described in the US Air Force's initiative in electrifying aerial vehicles [13, 139].

Both the severely reduced electrolyte conductivity and dramatically hampered solid state diffusion [140, 141] in high-power rechargeable Li-ion batteries currently limit commercial products to a minimum operational temperature of approximately –20 ºC [140, 141]. Such limitations can be circumvented by using EDLCs. Such alternative high-power electrochemical energy storage devices do not require solid state diffusion and permit a

stable operation with a much wider variety of electrolyte salts and solvents [11, 142]. Thus, they are of particular interest for further development and use at ultra-low temperatures [143, 144].

Supercapacitors have seen a major increase in attention in the past few years [11, 70, 109, 126, 142, 145-153]. The interest in these devices takes root in their ability to reach energy density levels that are orders of magnitude higher than solid-state capacitors while providing power densities much higher than any available battery [11, 142]. Supercapacitors have been shown to have cyclability of over 1,000,000 cycles [142] and in laboratory studies of ZTCs there has even been a case of increased performance after 10,000 cycles [116]. The current applications of these important devices include electric vehicles and HEVs, energy efficient industrial equipment, improving power quality, consumer electronics (e.g. camera phones, hand-held drills), and other applications requiring long cycle life, moderately high energy density, and charging within seconds or less [11].

For a given electrolyte, the energy storage characteristics of EDLCs are largely determined by the ability of their electrodes to adsorb a large quantity of ions under an applied potential [154]. Their power characteristics, in turn, are governed by the rate at which ions from an electrolyte solution can be delivered to, and adsorbed on, the available electrode surface area during charging [154].

Improving power density of EDLCs can be achieved by improving the rate of ion transport within the porous carbon electrodes [70, 116, 152, 155, 156], minimizing the ion diffusion distance [157], or by utilizing both approaches [158-160]. However, the overall electrochemical characteristics of the system should be carefully considered when approaching the synthesis routes of the various components. For example, by forming

large interconnected mesopores and minimizing, or altogether eliminating the micropores within the electrode materials, the average coefficient of ion diffusion within carbon can be enhanced, but at the expense of a greatly reduced volumetric capacitance and an increased amount of electrolyte needed to fill the enlarged electrode pore volume. With respect to the entire electrochemical cell, as the relative weight of electrolyte becomes higher than the weight of carbon, both volumetric and gravimetric energy density will be reduced. Therefore, while electrodes produced from highly porous electrodes such as carbon onions [70, 158], carbon nanotubes [70, 160] and graphene [156, 159] offer high power density to EDLCs, their excessive pore volume inevitably reduces the energy density of the fabricated devices. Similarly, a reduction of the electrode thickness from 200-300 µm [116, 152, 161, 162] to a few µm or below [158, 159] greatly reduces the average ion path length and thus dramatically decreases the characteristic charging time. However, this reduction leads to a major increase in the relative weight and volume of the inactive device components (such as metal foil current collectors and separator membrane) and thus will significantly reduce both the gravimetric and volumetric energy density of the fabricated devices.

Commercial EDLCs with activated carbon electrodes and electrolyte composed of 1 M solution of tetraethylammonium tetrafluoroborate (TEA-BF_4) salt in acetonitrile (AN) solution fail to operate at temperatures below approximately –40 ºC [144]. In a prior study our collaborators investigated electrodes utilizing commercial mesoporous activated carbon with an average pore size of 3.6 nm in an electrolyte consisting of TEA-BF_4 salt in AN mixed with 25 vol. % of low freezing point co-solvents, such as methyl acetate (MA), methyl formate (MF) and 1,3 dioxolane (DIOX) in order to extend the low

temperature limit of EDLC operation. The relatively large pore size of activated carbons is expected to allow fully solvated ions to move within the carbon pores at low temperatures, where thermal energy could be too low for distortion or partial removal of ion solvation shells. The studies demonstrated stable operation at temperatures as low as –55 ºC [143, 144]. When the temperature was further lowered, a significant decrease in the electrolyte conductivity of these devices and a respective decrease in the maximum operating frequency were observed. Additionally, even when the cells were discharged slowly they could not demonstrate a specific electrode capacitance above ~40 F g^{-1}, which is only 50 % of commercial EDLCs at room temperature (~ 80 F g^{-1}). The low capacitance is explained largely by the large carbon pore size, which was shown to demonstrate significantly inferior capacitance than small micropores [121, 163-165].

This study will demonstrate that strictly microporous carbons may allow for rapid ion transport and excellent capacitive storage characteristics at temperatures as low as –70 ºC.

3.2 Results and Discussion: Material Characterization

3.2.1. Microscopy

Formation of uniformly sized micropores in activated carbons is challenging. Microporous carbide-derived carbons [121, 166-169] exhibit narrow pore size distribution but suffer from a tortuous pore shape, which has been shown to affect the rate of ion transport in micropores [153]. In contrast, the use of sacrificial zeolite templates for porous carbon synthesis allow formation of straight ordered and interconnected micropores. In our studies we thus selected to use the robust zeolite lattice as a template for microporous carbon synthesis. Microporous ZTC were prepared by the decomposition of acetylene

(C_2H_2) precursor into a carbon coating on the internal surface of a zeolite NaY powder template. In contrast to most of the prior work, however, we performed carbon deposition at low pressures (2-5 Torr) and relatively low temperature (700 °C) to achieve a high carbon coating uniformity [115, 116]. Two ZTC samples were additionally heat-treated at 800 °C and 900 °C for one hour in a dynamic vacuum (flowing Ar) environment. Removal of the zeolite NaY powder template was achieved via etching in hydrofluoric acid, followed by removal of the remaining impurities using sulfuric acid and a final powder filtration, and washed with water until achieving a neutral pH.

The retention of the zeolite shape by the ZTC particles was confirmed by SEM and TEM studies (figure 3.1 A-C). In contrast to our previous study in which low pressures were not employed [126], a highly uniform structure of ZTC was attained (figure 3.1 B, C) with no macropores or thick multi-layered graphitic regions visible by TEM. Our previously reported X-ray diffraction (XRD) studies revealed a higher degree of pore alignment in ZTC samples heat-treated prior to zeolite etching [116].

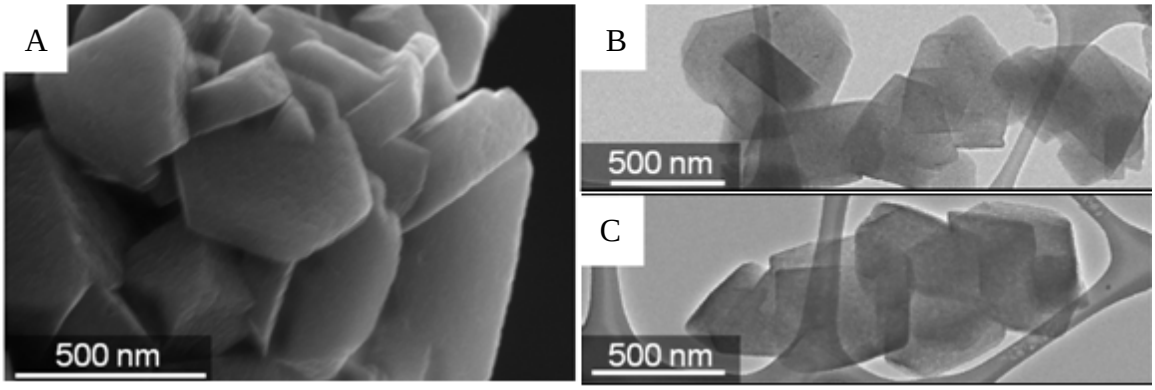

Figure 3.1. Microstructure of synthesized zeolite NaY – templated carbon powder: (A) SEM and (B, C) TEM micrographs of carbon particles indicating replication of zeolite shapes and high uniformity of carbon deposition.

3.2.2. Gas Sorption

The annealing treatment not only reduced the defects in carbon and assisted in the retention of the zeolite pore shape [116], but also increased the SSA and the total pore volume of ZTC as revealed by our investigation utilizing nitrogen sorption measurements (figure 3.2 A, B). The isotherms show virtually no hysteresis, indicative of the absence of the capillary condensation phenomena and the lack of significant mesopore content [170]. NLDFT calculations indicated that all three ZTC samples consist mostly of micropores and exhibit moderately high SSA (figure 3.2 A, B) and pore volume (figure 3.2 B). Figure 3.2 C displays the calculated pore size distribution out to ~30 nm to further demonstrate (in addition to the TEM data) that there is a uniform coating throughout the zeolite pore structure and the absence of remaining cavities as a result of an inhomogeneous coating of the zeolite.

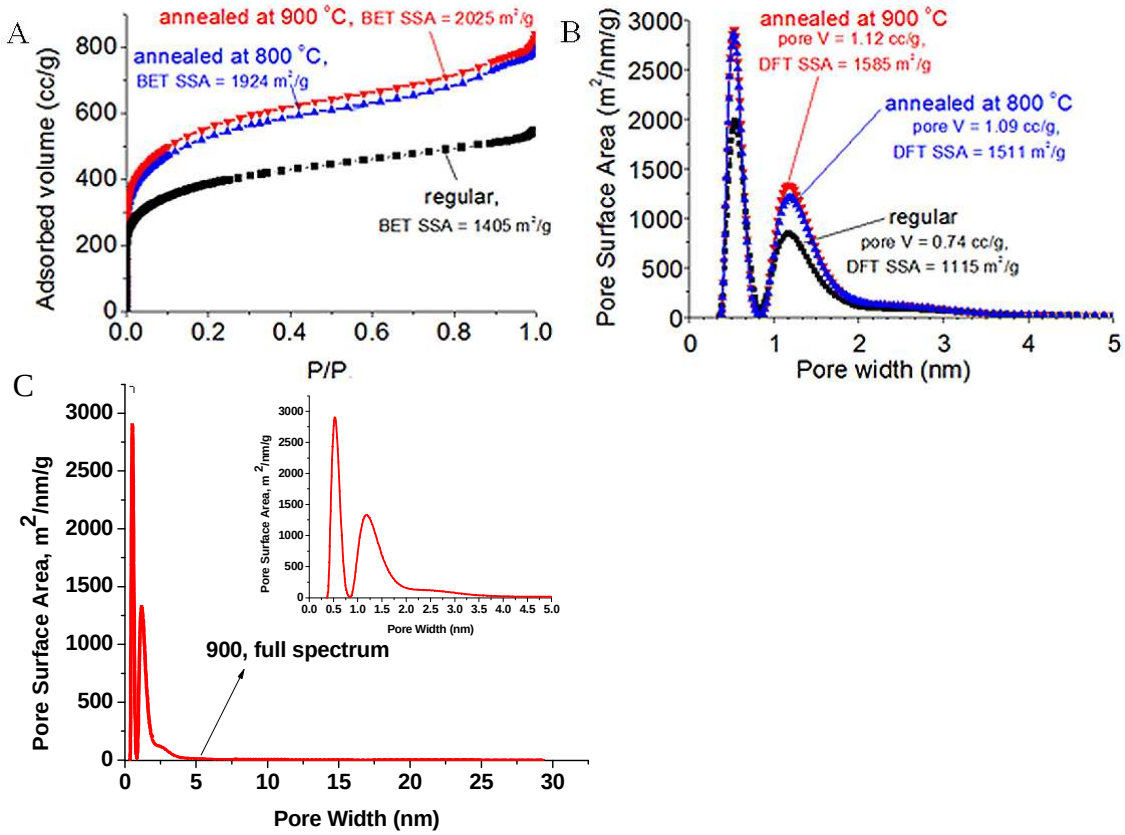

Figure 3.2. Porosity characterization of synthesized zeolite NaY – templated carbon powder: (A) N_2 sorption isotherms recorded at 77K and (B) pore size distribution in carbon calculated using NLDFT and (C) extended pore size distribution demonstrating uniformity of carbon deposition within the zeolite particle.

3.3 Results and Discussion: Electrochemical Characterization

Electrochemical characterization of ion transport and electroadsorption in microporous carbons were performed in both standard electrolyte (1 M TEA-BF_4 in AN) and in electrolyte consisting of a 0.5 M solution of spiro-(1,1')-bipyrrolidinium tetrafluoroborate (SBP-BF_4) salt in a 1:1 mixture of AN and MF. We chose MF as a co-solvent for the present study due to its low melting point (–100 °C) in addition to it having a moderate dielectric constant (ε=8.5) and low viscosity (0.319 cP at 29 °C). Our interest in studying a system consisting of SBP-BF_4 salt rather than the common TEA-BF_4 lays in SBP-BF_4's higher ionic conductivity at low temperatures, observed when used with pure propylene carbonate solvent in an EDLC configuration [171] and a general lack of investigations into

its electrochemical behavior in EDLCs. Maintaining a salt concentration at least as low as 0.5 M was used to avoid salt precipitation at low temperatures, as previously observed in EDLCs with TEA-BF_4 salt below –40 ºC.

3.3.1 Conductivity Tests

The ionic conductivity of the standard commercial electrolyte is higher than that of SBP-BF_4 in 1:1 AN:MF from room temperature down to approximately –55°C, where the standard electrolyte freezes (figure 3.3). As expected, increasing the salt concentration supports a higher conductivity. However, if the electrolyte concentration is too high, the equivalent series resistance (ESR) of EDLCs steadily increases over time at such low temperatures due to salt precipitation on the carbon electrode surface [143, 144].

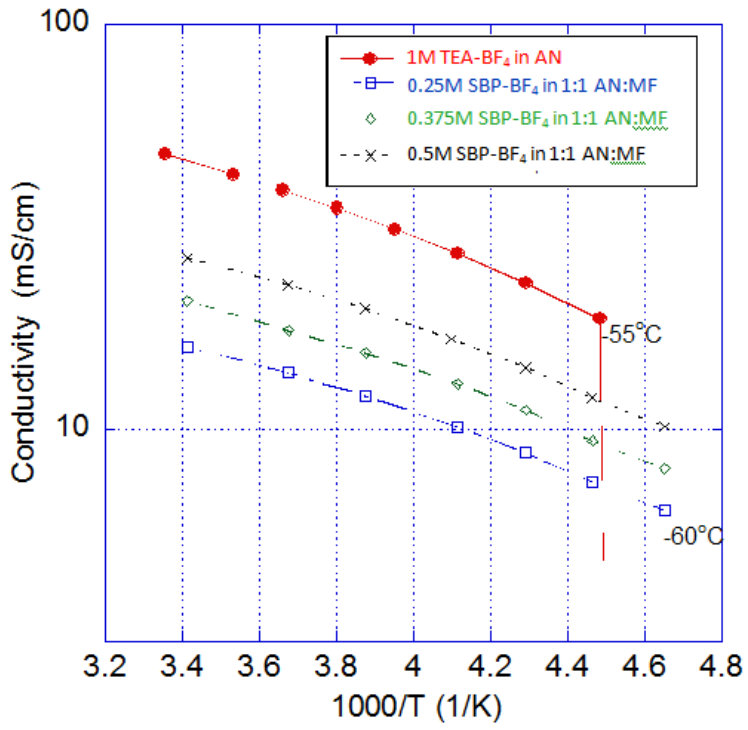

Figure 3.3. Conductivity of conventional (1 M TEA-BF_4 salt in AN) and newly developed (0.25M, 0.375M and 0.5M solutions of SBP-BF_4 salt in a 1:1 mixture of AN and MF) electrolytes as a function of temperature. The rapid drop in conductivity of the conventional electrolyte is visible at below –55 ºC.

3.3.2 Room Temperature CV and EIS

Cyclic voltammetry measurements at the sweep rate of 1 mV s^{-1} showed the high specific capacitances for all ZTC samples when measured at room temperature (RT) in both electrolytes (figure 3.4 A, B). The most disordered sample [116] (termed "regular" in the figures) consistently showed the highest capacitance (136-146 F g^{-1}) at 1 mV s^{-1} and the smallest capacitance retention at high current densities (figure 3.4 A, B). Prior studies revealed that defects and functional groups on the carbon surface may interact with both the ions and the solvent molecules in organic electrolytes, distorting the solvation shells and leading to the enhancement of specific capacitance normalized per unit area[70]. This could be due to both the presence of a reversible pseudocapacitive behavior [149, 172] and the closer approach of the ions to the electrode surface, either by reduction of the solvation shell thickness or partial desolvation through distortion of the shell [121]. A decreased charge separation distance is known to lead to higher capacitance, as observed in disordered microporous carbons [121].

The RT specific capacitance of carbons in both types of electrolyte was similar (within 10 %) (figure 3.4 A, B). Some samples (e.g., a "regular" and annealed at 900 ºC) showed marginally higher capacitance in the standard electrolyte, while others (e.g., the one annealed at 800 ºC) exhibited slightly higher capacitance in SBP-BF_4/AN:MF electrolyte. Such small variations are to be expected and rationalized by the complex electrode-electrolyte interactions affecting the specific capacitance. Parameters influencing the capacitance include, but are not limited to, the interplay between the carbon pore size and the size of the solvated and de-solvated ions [121, 163-165, 173], local curvature of the carbon surface [152, 164, 165, 174], interaction of the electrolyte with dopants

[109], and functional groups [148,150], and defects on the carbon surface [70]. Nonetheless, it appears that the higher conductivity of the standard electrolyte (figure 3.3) leads to slightly better ion transport properties and capacitance retention at higher sweep rates at RT (figure 3.4 A vs. B). It was also observed that the sample annealed at 900 ºC and possessed the most aligned pore structure (as revealed by our prior XRD measurements [116]) consistently showed the best capacitance retention, supporting our previous observations in aqueous electrolytes [116].

The RT frequency response of EDLCs made with either type of electrolyte was very good (figure 3.4 C, D). A maximum operating frequency f_{max} (the frequency above which less than 50% capacitance is accessible) of up to ~0.3 Hz is very high for electrodes consisting of a strictly microporous carbon. In fact, it exceeds that of mesoporous carbon electrodes having a significantly larger pore volume [175] and indicates fast transport of ions.

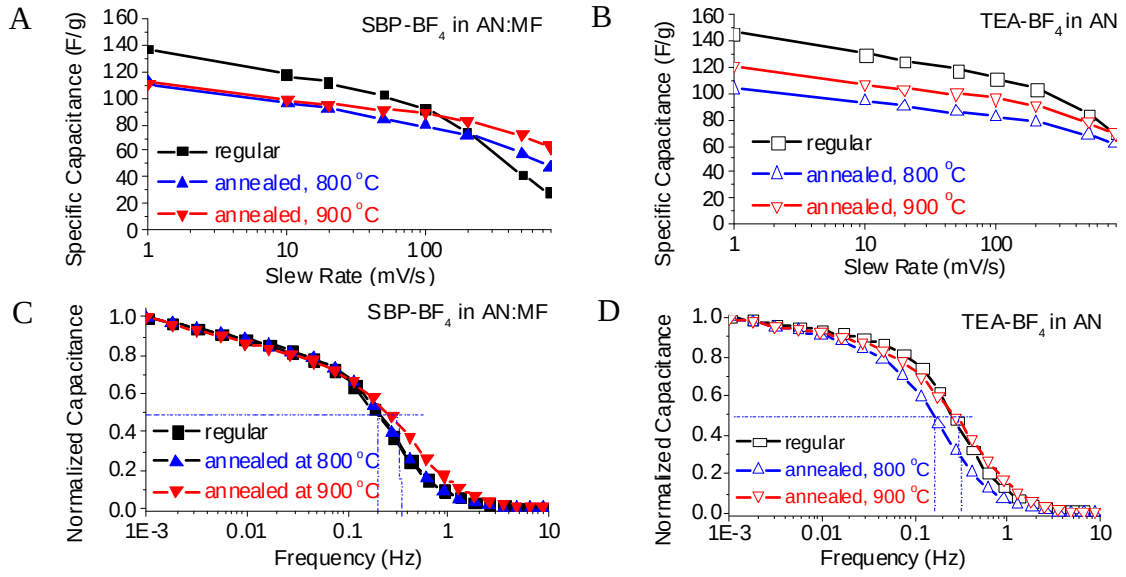

Figure 3.4. Room temperature performance of EDLCs in conventional (TEA-BF_4 in AN; hollow symbols) and newly developed (SBP-BF_4 in AN:MF=1:1; solid symbols) electrolytes: **(A, B)** specific capacitance calculated from the CV curves as a function of sweep rate; **(C, D)** frequency response of capacitances. Zeolite - templated carbons

synthesized at 700°C (regular and annealed for one hour at 800 and 900 ºC) were used in the EDLCs.

3.3.3 Extreme Temperature Studies

As the operational temperature is lowered to –20 ºC and –40 ºC the superior performance of SBP-BF_4/AN:MF becomes apparent (figure 3.5 A, B). At these temperatures the standard electrolyte consistently shows a smaller capacitance for all the ZTC samples, which is particularly evident at faster slew rates. While the conductivity of the standard electrolyte is higher at these temperatures (figure 3.3), its higher salt concentration and higher ion solvation energy likely limit its performance at temperatures below –20 ºC. When the operational temperature is further dropped to –60 ºC or below, the devices with a standard electrolyte cease to operate at meaningful levels (figure 3.5 C, D). Yet, the EDLCs based on ZTC electrodes and SBP-BF_4/AN:MF show outstanding performance. Due to the small pore size in ZTC, the electrode capacitances (up to 123 F g^{-1} at –60 ºC and up to 117 F g^{-1} at –70 ºC), and thus the energy storage characteristics of these EDLCs, are higher than that of most commercial carbon electrodes operating at RT (commonly 75-85 F g^{-1} [152, 162, 176]). The frequency response at –60 ºC (f_{max} in excess of 0.1 Hz for ZTC annealed at 900 ºC, figure 3.6) also exceeds that of commercial devices at RT (0.01-0.1 Hz, [143, 176]), which indicates their superior power characteristics.

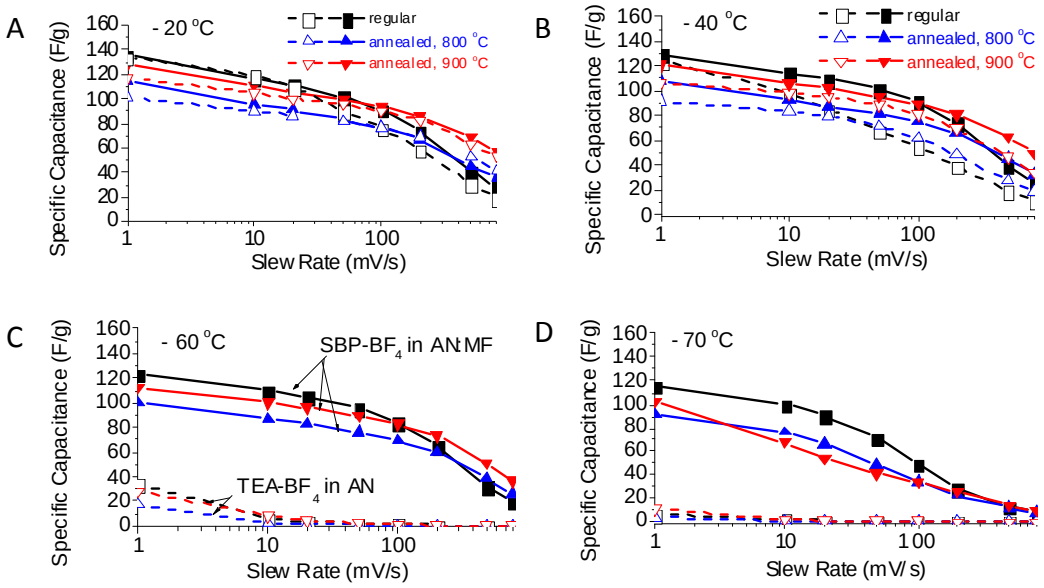

Figure 3.5. Specific capacitance of ZTCs synthesized at 700°C (regular and annealed for one hour at 800 and 900 ºC) in conventional (TEA-BF_4 in AN; hollow symbols) and newly developed (SBP-BF_4 in AN:MF=1:1; solid symbols) electrolytes calculated from the cyclic voltammetry (CV) curves of symmetric EDLCs as a function of sweep rate at (A) –20 ºC, (B) –40 ºC, (C) –60 ºC, and (D) –70 ºC.

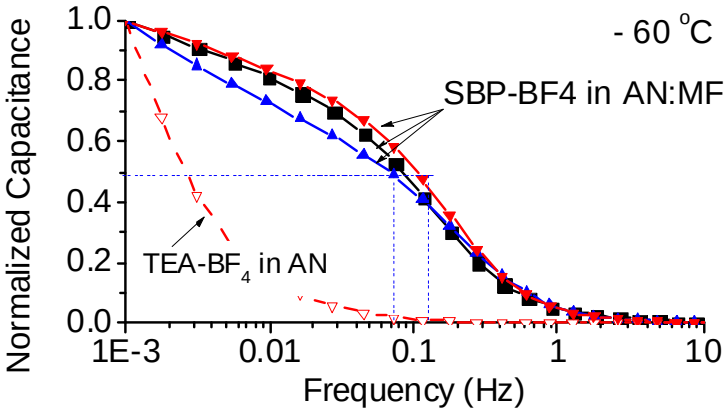

Figure 3.6. Frequency response of capacitances of ZTCs synthesized at 700°C (regular and annealed for one hour at 800 and 900 ºC) in conventional (TEA-BF_4 in AN; hollow symbols) and newly developed (SBP-BF_4 in AN:MF=1:1; solid symbols) electrolytes at –60 ºC.

Figure 3.7 compares the shape of the cyclic voltammograms of EDLCs with the two studied electrolytes at –70 ºC. In spite of the very low temperature the EDLCs based on ZTC electrodes and SBP-BF_4 / AN:MF electrolyte exhibit a nearly rectangular shape

of the curve, indicative of nearly ideal EDLC behavior and unobstructed access of the electrolyte ions to most of the available surface area. Indeed, the supercapacitor electrodes at –70 ºC retain 82-86% of their RT specific capacitance. In contrast, similar devices constructed with the standard 1 M TEA-BF_4 / AN electrolyte (figure 3.7) show a highly distorted curve and exhibit dramatically reduced energy and power storage capabilities. Thus, a careful design of electrolyte is needed for microporous carbon EDLCs' use at low temperatures.

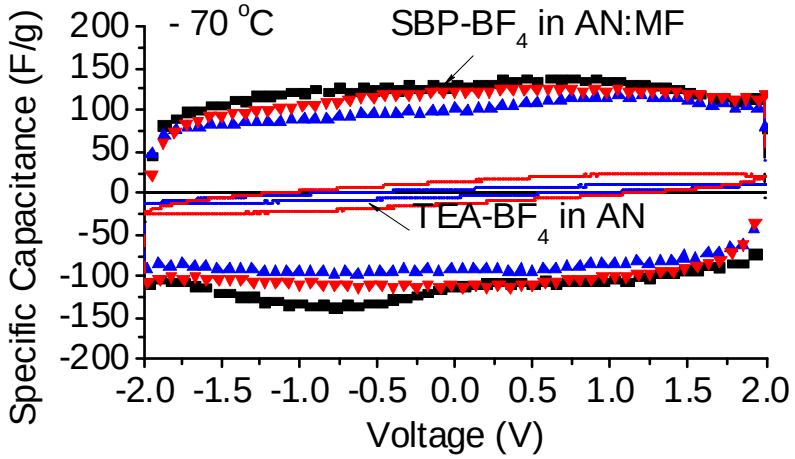

Figure 3.7. Cyclic voltammograms of zeolite - templated carbons synthesized at 700°C (regular and annealed for 1 hour at 800 and 900 ºC) in conventional (TEA-BF_4 in AN; hollow symbols) and newly developed (SBP-BF_4 in AN:MF=1:1; solid symbols) electrolytes at a slew rate of 1 mV s^{-1} recorded at -70 ºC.

3.3.4 Pore Size Impact at Extremely Low Temperatures

Figure 3.8 compares the low temperature performance of mesoporous carbon (having an average mesopore size of ~3 nm and a specific capacity of 65 F/g at room temperature) with that of ZTC in SBP-BF_4 / AN:MF electrolyte. At temperatures as low as -60 °C (figure 3.8A) and -70 °C (figure 3.8B) ZTCs show three times higher specific capacitance. In spite of having a smaller pore size, ZTCs demonstrate higher capacitance retention at faster sweep rates (figure 3.8C) and a better overall performance (figure 3.8D). The ability of the ZTCs to outperform the performance of a mesoporous carbon is

not without limits. In our studies the ZTC particles were around 0.5 μm in size. If these particles became too large and the path for ions to travel thus increased, decay in frequency response would ensue. It is important to design the particle size so that it is appropriate for the frequency response required in various applications. From these experiments we conclude that the high performance at such low temperatures cannot be solely attributed to the novel electrolyte but necessitates a carbon that can efficiently facilitate the rapid electroadsorption of the salt ions onto its surface.

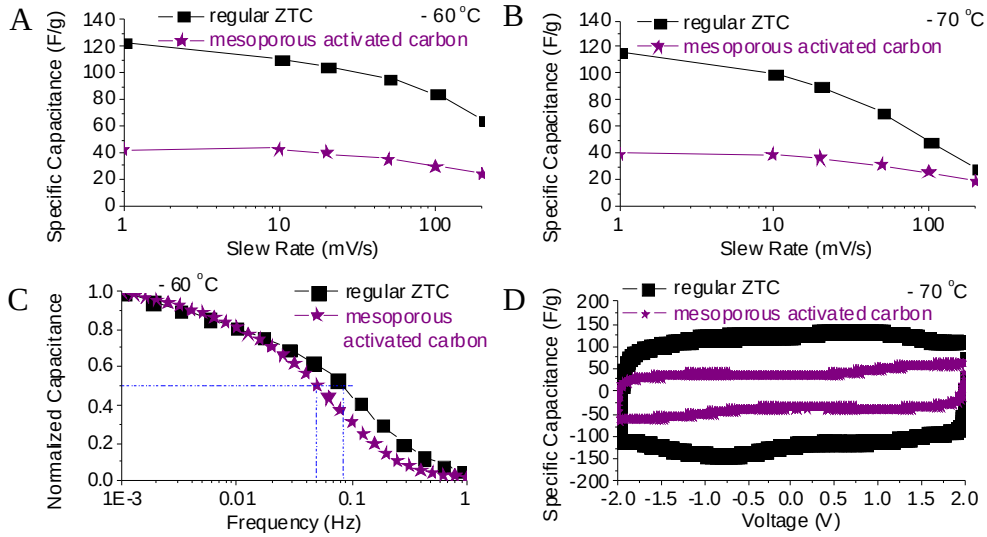

Figure 3.8. Comparison of the low-temperature performance of EDLCs based on ZTC and mesoporous activated carbons: specific capacitance calculated from the CV curves as a function of sweep rate at (A) -60 ºC and (B) -70 ºC; (C) Frequency response of carbons and (D) cyclic voltammograms at a slew rate of 1 mV/s recorded at -70 ºC. Zeolite Y - templated carbons synthesized at 700°C and CECA's Acticarbone activated carbon were used in the EDLC electrodes, while SBP-BF_4 in AN:MF=1:1 solvent was used as electrolyte.

3.3.5 Salt Effects CV and EIS

In order to reveal the effect of the salt dissolved in the same low temperature solvents, figure 3.9 compares the performance of TEA-BF_4 vs. SBP-BF_4 in 1:1 AN:MF solution. As can be seen in the data, the positive impact of the SBP cations is evident at low temperatures. Both the value of the specific capacitance and the capacitance retention

at -60 ºC is noticeably better when using SBP-BF_4 as compared to the standard commercial TEA-BF_4 in the same solvent. This impact may stem from an increased energy of solvation for the TEA-BF_4 becoming more evident at lower temperatures as the thermal energy of the system is reduced. This increased energy barrier makes it more difficult to distort or remove the solvation shell and impedes the ability of the fully or partially solvated ions to efficiently organize into the most possibly compact layer. Improved ion mobility and resistance is further evinced by figure 3.9B which demonstrates the lower specific capacitance and increased ionic resistance for the TEA-BF_4 salt at -70 °C.

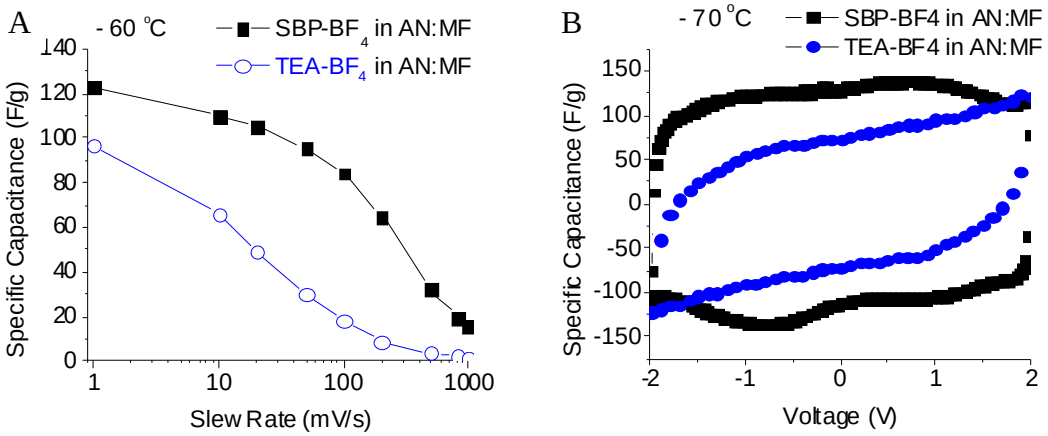

Figure. 3.9. Effect of the cation on the low-temperature performance of EDLCs utilizing AN:MF=1:1 solvent : specific capacitance calculated from the CV curves as a function of sweep rate at **(A)** -60 ºC and **(B)** cyclic voltammograms at a slew rate of 1 mV/s recorded at -70 ºC. Zeolite Y - templated carbons synthesized at 700°C were used as electrodes, and TEA-BF_4 and SBP-BF_4 salts were used in electrolyte.

The observed behavior in our electrochemical cells can be explained by addressing the multiple factors involved in the migration of dissolved ionic species in the pores of the ordered microporous carbon. As we decreased the temperature of our electrolytes we observed a reduction in conductivity. Such conductivity is known to be proportional to the ion charge (q), the concentration of ions (N) and their mobility (μ):

$$\boldsymbol{\sigma = qN\mu} \tag{3.1}$$

One factor attributed to the decreased conductivity is the decreased mobility of the solvated ionic species as a result of the increased viscosity, which in turn increases the drag on the solvation shell of the dissolved ionic species. If we approximate moving ions as spheres and use a macroscopic model, then we can utilize the relationship between viscosity and the force opposing a macroscopic sphere's movement that should follow the Stokes relationship:

$$\boldsymbol{F = 6\pi r\eta v} \tag{3.2}$$

The force (F) on the sphere experiencing drag is a function of the radius (r), viscosity (η), and velocity (v). While the magnitude of the force is a matter of debate as a result of the assumptions in the derivation, the relationship indicating an increase in force with an increase in the viscosity is believed to be applicable to the motion of ions in the electrolyte [177]. Another important relationship to take into account, more easily related to the conductivity (as seen in equation 3.1), is between the viscosity and the mobility [177]:

$$\bar{u}_{abs} = \frac{1}{6\pi r\eta} \tag{3.3}$$

This relationship predicts that the absolute electrochemical mobility ($\bar{u}_{abs}$) is inversely related to the viscosity (η) of the medium and the radius of the solvated ion (r).

The next factor to take into consideration is the thermal energy, which affects two related factors – ion pairing and the solvation shell. Bjerrum investigated the concept of ion pairing in solution and provided a metric for their formation that relies on the following relationship:

$$l \propto \frac{1}{T} \tag{3.4}$$

l can be defined as the distance that is sufficient for the columbic interaction between oppositely charged ions to stick together to form a neutral pair of ions. As temperature (T) is decreased the distance allowing for ion-pair formation is increased leading to increased probability for ion-pair formation [177]. Once the oppositely charged ions form a pair and share a solvation shell they no longer participate in the ion conductivity, which decreases the overall concentration of mobile ions in the solution (N, in eq. 3.1). The fraction of ions that are associated into ion pairs (θ) can be estimated using the following relationships [177]:

$$\theta = 4\pi n_i^0 \left(\frac{z_+ z_- e_0^2}{\varepsilon kT}\right)^3 \int_2^b e^y y^{-4} dy \qquad (3.5)$$

$$b = \frac{z_+ z_- e_0^2}{\varepsilon akT} = \frac{2l}{a} \qquad (3.6)$$

$$y = \frac{2l}{r} \qquad (3.7)$$

The different parameters include the ion concentration (n_i^0), the charge numbers (z), electron charge (e_0), dielectric constant (ε), Boltzmann's constant (k), l (equation 3.4), the distance of closest approach of a pair of ions or ion size parameter (a), and the distance from the ion over which the probability of pairing is examined (r). Bjerrum tabulated the integral in equation 3.5 for various values of b. Equations 3.5-3.7 and the tabulated integrals indicate that as the temperature is reduced the fraction of ion pairing is increased along with a decrease in the conductivity.

We shall note that the formation of the solvation shell is driven by the intermolecular forces between the polar solvent and the ionic species. This interaction, however, is perturbed if the thermal energy is provided at higher temperatures. In

contrast, as the temperature (and thermal energy of ions in the solution) is reduced the probability to remove or distort the solvation shell becomes smaller. Since the migration of ions into the small pores of ZTC requires significant distortion (partial removal) of the solvation shells one would expect reduced capacitance at low temperatures, as experimentally observed (compare figure 3.4 and figure 3.5).

Once the ion has transported into the ordered pore structure of the ZTC, in order to allow for its progression through the pore it must overcome a variety of energy barriers. The synthesis method used to produce ZTCs results in a controlled morphology and fairly regular chemistry as compared to activated carbons derived from organic precursors like coconut shells. The interaction of ions with surface atoms in the ZTC pore are likely fairly periodic, but the ion may also encounter various defects resulting in increased energy barriers for continued transport. This is schematically demonstrated in the figure 3.8 below. According to the Arrhenius equation for thermally activated processes, the diffusion rate of an ion should follow:

$$k = Ae^{-\frac{\Delta G}{RT}} \qquad (3.8)$$

Where ΔG is the energy barrier faced by a partially desolvated ion during its transport within the ZTC pores. Reduced thermal energy reduces the ion transport rate according to equation 3.8. We shall further note that as a result of the strong exponential dependence of the ion transport rate on the height of the barrier, the presence of higher energy barriers (like those that might be afforded by defects) becomes particularly detrimental at lower temperatures.

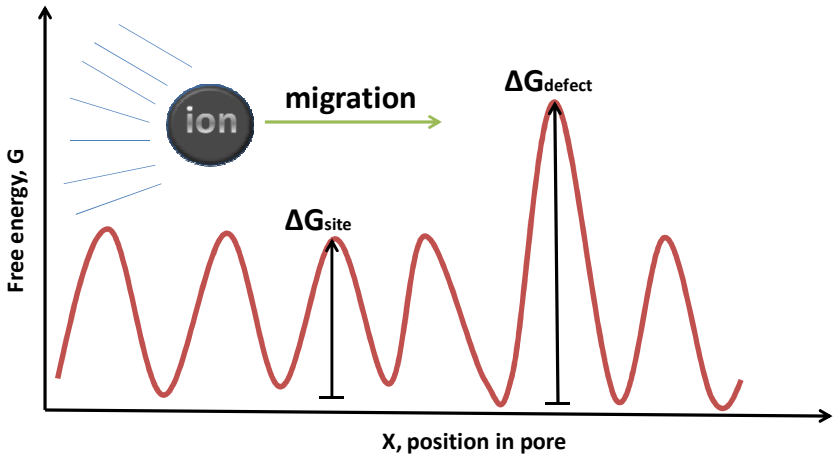

Figure 3.10. Schematic illustrating the effect of energy barriers associated with migration of ionic species within the pores of the carbon material. Interaction of ions with surface atoms can be described as a periodic potential, while the interaction of ions with various defects leads to higher and non-periodic energy barriers.

3.4 Conclusions

In summary, the low pressure decomposition of acetylene precursor onto a sacrificial zeolite template resulted in the formation of uniform microporous carbons with high surface area and high energy and power performance characteristics when used in EDLCs with organic electrolytes. At room temperature the electrodes produced with the synthesized microporous ZTC exhibited excellent ion transport and electro-adsorption characteristics with capacitances in the range of 100-146 F g^{-1} and a maximum operating frequency of up to 0.3 Hz in organic electrolytes. The studies further demonstrated that mesopores, which commonly reduce the specific and volumetric carbon capacitance, are not needed for high-power EDLC operation even at ultra-low temperatures. The synergetic use of microporous ZTC and carefully designed electrolyte (0.5 M SBP-BF_4 in 1:1 AN:MF) demonstrated an unprecedented combination of high specific capacitance, rapid charging/discharging ability and high energy density characteristics at –70 ºC (up to 86 % of the energy density available at room temperature). These results open up many opportunities for high-energy electrochemical capacitor utilization for energy efficient

applications in space vehicles, high-altitude aerial vehicles, mountainous and Polar regions, and facilitating the efficient utilization of renewable energy resources.

CHAPTER 4

ZEOLITE-CARBON COMPOSITE CHARACTERISTICS AND THEIR ELECTROCHEMICAL BEHAVIOR IN LEAD-ACID BATTERIES

4.1 Introduction

LABs have been in use for over a century. They have an established infrastructure that allows for the highest recycling rate of any other battery. Their energy, power, cycle life, self-discharge rate, and cost have resulted in their application in areas such as submarines [178], uninterruptable power supplies [179], military vehicles (ground and air) [180, 181], golf carts [182], lift-trucks [182], miner's caps [183], and, for over a century, in automobiles.

Today, with the growing interest of applying LABs to HEVs and integrating LABs into a smart electric grid, there are very different demands being placed upon LABs. As compared to SLI batteries, in the HEV there will be higher exposure of the LAB to a partial state of charge (PSOC) and high rates of charge and discharge, resulting in an operation state termed high-rate partial state of charge (HRPSOC). This operation results in an increase in inefficient charge-discharge processes leading to a gradual build-up of lead sulfate on the negative active material (NAM), which is often attributed to the failure of the LAB, termed "sulfation [180]." Main causes attributed to the failure of the NAM are prevention of the electrolyte to reach the active surface by lead sulfate pore filling and isolation of active material from the current source by insulating lead sulfate [16]. To address these issues, research efforts have varied from adding multiple lugs to the

plates in order to distribute the potential more evenly (and the lead sulfate along with it) [17], and using conductive and non-conductive additives [18-20].

Many additives have been investigated for application in LABs, and there are key issues that must be met by such additives. These include stability in the electrochemical environment, good mechanical strength, geometrical shape assisting formation of a conductive network, low cost, and low weight. Additives that have been examined in the positive-active material (PAM) have included carboxymethylcellulose [184], carbon black [184], silica gel [184], diatoms [185], zeolite [19], titanium silicide [16], titanium wire [16], titanium dioxide fibers [16], graphite [186], carbon fibers [186], and various other additives [187,188]. Many investigations into the NAM have been undertaken and they have included hollow glass microspheres [187], expanded graphite [189], flake graphite [189], micro-fiberglass [189-190], carbon nanotubes [19], sodium sulfate [191], zeolite [192], and various other additives. Some of these materials have resulted in marked improvement in one metric or another (e.g. capacity, or cycle life) while utilizing only a few weight percentages (often going above this amount results in a decrease in performance and dispersion issues). It should be noted that both conductive and non-conductive additives have shown some level of success. Explanations for why the enhancements occur include securing a conductive network between sulfate coated active material and the rest of the network, acting as electrolyte reservoirs, increasing the surface area and porosity, acting as electro-osmotic pumps for the electrolyte, acting as nucleation sites for the lead sulfate, and for sterically hindering the growth of lead sulfate crystals. The effects various additives have on different metrics indicate that selection of materials should be based on the type of application for the LAB (e.g. SLI vs. HRPSOC) and their ability to prevent or delay failure of the NAM by

addressing the above developments. In order to allow for LABs to perform well under HRPSOC conditions, additives improving the majority, if not all, metrics of LABs must be developed and the mechanisms for their improvement must be investigated.

There have been several studies utilizing carbons, silica and zeolite as additives in NAM with various levels of success [19, 193, 194]. These previous studies often did not characterize various aspects of the additives which they were employing and the reason for their use was not always made clear. For example, when using a conductive additive like carbon, the fact that it may very well be hydrophobic and not facilitate the conduction of electrolyte to active material sites was not posed in the majority, if not all, of the additive investigations [18, 19, 186, 195, 196]. In some of these papers the idea of using an additive as an acid reservoir was suggested, and for that reason silica gel was used in a few studies, with some positive results, e.g. high rate capacity improvement, but no improvement in cycle life [196]. Some researchers suggested that to improve electrolyte transmission into the bulk of the electrode increased porosity was of importance, which could be developed through the use of porous additives. Finally, some researchers suggested that conductive additives, like graphite, may assist in the transmission of electrolyte to the core of the electrode through an electro-osmotic pump mechanism. It seems almost none of the materials tested were investigated in terms of their affinity for the electrolyte species and, therefore, further studies examining the effect of this characteristic are necessary. One reason for examining the affinity for the solvated ions, is the possibility that electrolyte can only sluggishly penetrate hydrophobic particles, impacting power density and, in some cases, causing impermeability resulting in reduced capacity altogether. When using zeolites or silicas with high surface area and an unknown

nature of hydrophilicity the same problems can arise. The fact that they are insulating indicates it is very likely that they are not assisting the system to overcome the buildup of insulating lead sulfate.

In our current investigation we explore the impact of a composite particle containing multiple characteristics of interest when it comes to LABs. The particle was inspired by recent work done in electrochemical capacitors. Record-breaking combinations of specific capacitances and power density have been reached in the past few years by using templated carbons in acetonitrile and sulfuric acid electrolytes. There have also been assertions that the success of carbon additives in LABs is primarily due to the high capacitance afforded by the carbons. If the latter hypothesis is true, then employing a zeolite-templated carbon in a sulfuric acid environment found in the LAB could result in increased performance. An interesting aspect of ZTCs is that they are thought to be hydrophobic [197], which could hamper their contribution to mobilizing electrolyte into the active material, especially at the high rates seen in HRPSOC operations. On the other hand, zeolite Na-Y is known to be hydrophilic and as such could be quite helpful in maintaining irrigation of the active material. A hybrid between the two materials might be extremely useful. This would provide the stability and hydrophilicity of zeolite while improving the conductivity via the carbon component. For that reason we have synthesized a particle consisting of zeolite coated with carbon, with high surface areas, implying that the pores of the zeolite are not obstructed by the carbon. The result is a zeolite-carbon composite with high potential for improvement of LABs.

4.2 Results and Discussion: Material Characterization

4.2.1 Microscopy

Scanning electron and transmission electron microscopy were utilized in order to examine the morphology of the ZCC particles. The resulting micrographs are displayed in figure 4.1. The SEM images indicate that the ZCC has a similar morphology to the zeolite structure as previously demonstrated for low pressure CVD (LPCVD, as in our study) and CVD of carbon on zeolite NaY templates [22, 116, 198]. The morphology consists of particles mostly in the size range of 0.5 to 1 μm and mostly smooth surfaces. Some rough features and less than perfect particles are seen in the TEM and may be attributed to the ball milling combined with the low deposition time which may lead to a destruction of some of the structure, but on a larger scale, as shown in the SEM images, many of the particles maintain the morphology conferred by the zeolite NaY template.

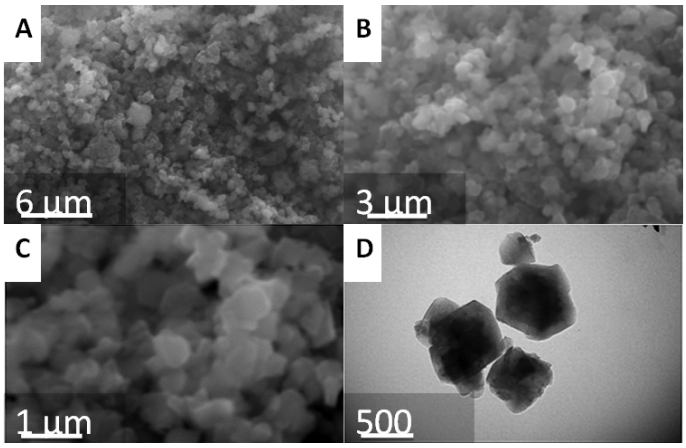

Figure 4.1. Microstructure of synthesized zeolite-carbon composite particles: (A,B,C) SEM and (D) TEM micrographs of zeolite-carbon composite particles showing morphology similar to that of zeolite and ZTC.

4.2.2 TGA & Hydrophilicity Testing

TGA analysis of the zeolite-carbon composite particles was undertaken to examine the moisture content and carbon to zeolite ratio post partial etching of the zeolite-carbon composite particles. In order to probe the moisture content of the material, nitrogen was flowed without an oxidant to high temperatures so that the moisture content of the CZ particle could be examined. The plateau (see figure 4.2) measured as time progressed that was reached at high temperatures was used as the point of reference to the initial mass in order to determine the moisture content. Using this method an approximate 14% of moisture was registered for this sample. Such a large content of moisture seems to indicate the hydrophilic nature and high surface area of the particle was maintained and not adversely affected by the etching process or the deposition of the carbon, as templated carbons have previously been shown to have a hydrophobic nature [197]. For comparison, it seems that from (unpublished) data ZTCs often have 10% or less of retained moisture.

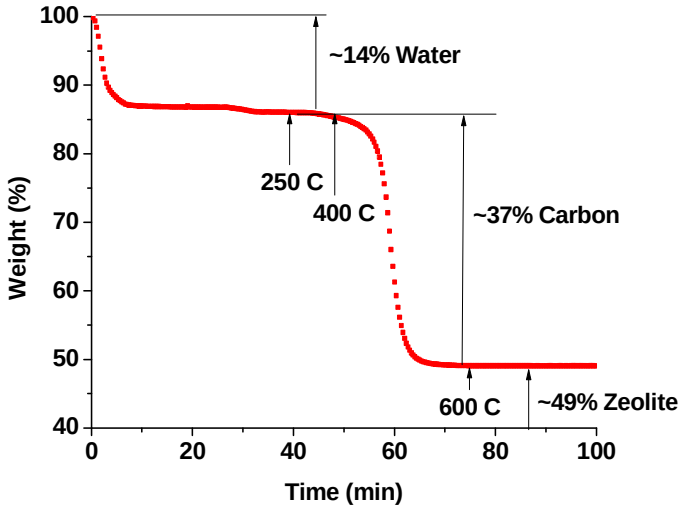

Figure 4.2. TGA demonstrating the weight content of the zeolite-carbon composite particles. The particles have significant moisture content due to hydrophilicity, and an

increased zeolite/carbon ratio as compared to ZTC due to the partial etching of the zeolite.

Once the content of moisture was recorded, the flow of oxygen gas was initiated along with the oxidation of carbon. At longer times and higher temperatures, a plateau was reached and an approximate measure of the carbon to zeolite ratio was ~0.75. A previous unpublished study by Kajdos indicated that the carbon to zeolite ratio in the same system should result in a 0.21 ratio of carbon to zeolite and Kyotani's study found similar C/Z ratios in a different deposition system with zeolite NaY [22], indicating that partial etching of the zeolite was obtained.

In order to further examine the hydrophilicity of the carbons synthesized, water sorption studies were undertaken. The tests involved evacuating the materials from moisture and then gradually increasing the vapor pressure and observing the uptake. The results are shown in figure 4.3. The investigations confirmed the increased hydrophilic nature of the ZCC materials as compared to the hydrophobic ZTC. The ZCC begins to adsorb moisture at much lower partial pressures as compared to the ZTC and requires much lower partial pressures to completely desorb the moisture from the pores. These results indicate the increased affinity towards moisture conferred upon the ZTC by the partial removal of the zeolite template.

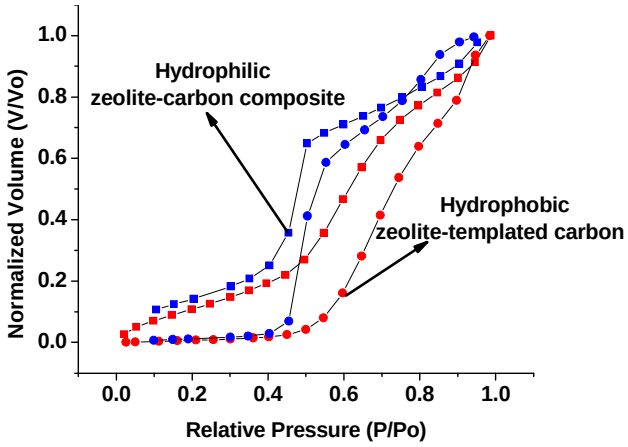

Figure 4.3. Water sorption isotherm of ZTC and ZCC (red=sorption, blue=desorption). The hydrophilic material begins adsorbing moisture at much lower pressures and requires lower pressures to empty the pores.

4.2.3 Gas Sorption

Sorption studies, utilizing several probe gasses, were used to examine the starting zeolite, the synthesized composite, and the resulting electrode materials. These studies were meant to provide insight into the available surface area and pore structure of the materials. Figure 4.5 displays data obtained by using Ar gas as a probe at liquid Ar temperatures (87 K). In figure 4.5A a type 1 isotherm for zeolite is shown indicating the high micropore content. Using an NLDFT model developed for cylindrical pores as expected from zeolite Na-Y, a pore size distribution was derived in figure 4.5B. The distribution shows the characteristic peak as expected from the crystal structure of zeolite resulting in an extremely tight pore size between ~0.4 and ~0.9 nm with a majority at ~0.7 nm. Once partial etching was completed the isotherm evinced a new development (figure 4.5A). The isotherm contained a clear hysteresis between the adsorption and desorption (also known as capillary condensation) branches indicating the development of mesoporosity. The model was applied again, as shown in figure 4.5C. It is important to keep in mind that developing an NLDFT model for such a partially etched ZCC is

difficult and so the distribution is not simple to estimate. As is shown later, the surface area is underestimated as compared to the BET model, which is important to keep in mind when analyzing the data. The mesoporosity and NLDFT model provide clear evidence that an increase in the breadth of available pore size was demonstrated, with a significant portion of micropores and a smaller volume of mesopores under 4 nm in size per the model's description. The isotherms were then used to calculate the BET specific area as shown in table 4.1, and an increase in available surface area was observed upon partial etching of the zeolite template.

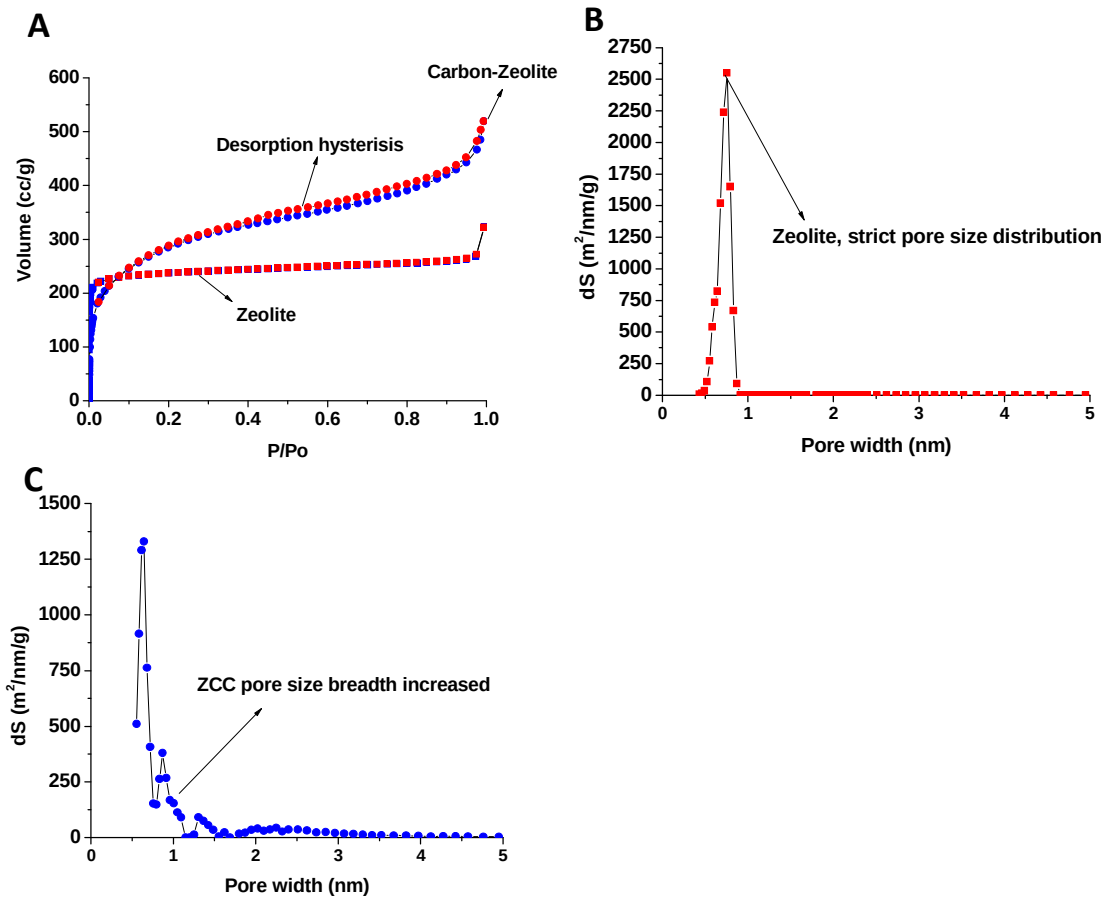

Figure 4.4. A) Argon sorption isotherm of zeolite NaY and ZCC at 87 K. B) Pore size distribution of Zeolite NaY as derived from the sorption isotherm in conjunction with an NLDFT model developed for Zeolites/cylindrical pores. C) Pore size distribution of ZCC as derived from the sorption isotherm in conjunction with the NLDFT model developed for Zeolites/cylindrical pores.

Table 4.1. Specific surface area as calculated from the sorption isotherms for the respective samples using Argon sorption and multi-point BET.

Sample	BET SSA
Zeolite Na-Y	**835.2 m^2/g**
Zeolite-carbon composite (post etching)	**910.6 m^2/g**

The accessible surface area of the electrode materials was studied using N_2 sorption studies and liquid N_2. All electrode materials demonstrated increased BET specific surface areas as a result of the incorporation of zeolite, ZCC, and FZCC (figure 4.6). In the case of the ZCC additive there appears to be a higher increase in the surface area that was not expected. During mixing of the various components of the electrode material lead sulfate crystals are developed by the addition of sulfuric acid to the lead oxide mixture. It is possible that the stronger affinity of the FCZ resulted in development of lead sulfate crystals within the pore and between particles leading to a reduction of the surface area. In addition, as the concentration of carbon was increased in the case of 2X ZCC, stronger agglomeration may have taken place with subsequent growth of lead sulfate in the cavities within these agglomerates causing a reduction of surface area as compared to the case of the ZCC.

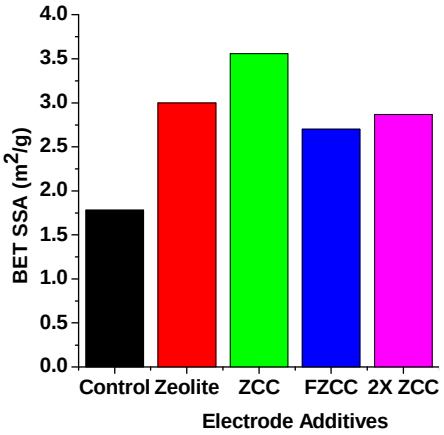

Figure 4.5. SSA as derived via multipoint BET for the NAM with the following compositions: control, zeolite-carbon composite, functionalized zeolite-carbon composite, and 2X zeolite-carbon composite.

4.3 Results and Discussion: Electrochemical Characterization

4.3.1 Capacity Tests

In order to study the effect of the various additives on the electrochemical performance of the electrode materials, the capacity of lab-type LAB cells were studied using Arbin and Maccor potentiostats. The measurements ranged from very slow discharge rates (~C/20, discharge over time periods of approximately 20 hours) to fairly high rates of discharge (~4C).

The C/20 tests revealed the strength of the novel materials with respect to increased active material utilization. Despite the increase in mass of carbon, which presumably does not involve Faradaic reactions, there is a significant increase in the capacity of the cells indicating an enhancement in active material utilization. The addition of hydrophilic and insulating zeolite revealed that even with a possible increase in supply of fresh electrolyte to sites of reaction, a reduction in capacity is observed. This phenomenon points to the importance of not only having a material of hydrophilic nature,

but the importance in maintaining conductivity when attempting to utilize more of the active mass (Pb).

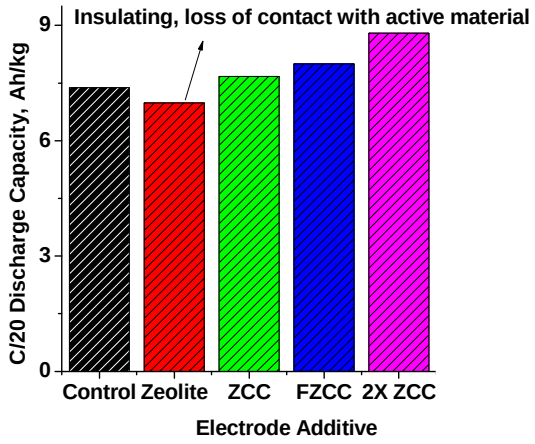

Figure 4.6. C/20 capacities of LABs consisting of various wt. % loading of the novel composite particles under investigation. The novel particles all appear to increase the capacity of the LAB under low current conditions. The insulating particle, despite its hydrophilicity, degrades the capacity under low current conditions.

The next set of tests was used to examine the effect of the additives on the ability of the cell to withstand increased discharge rates. As with the C/20 studies, the novel additives appeared to result in increased capacities at all discharge rates, low and high, indicating that additives do not reach a limit with respect to diffusion of sufficient electroactive ions or a significant reduction of conductivity. Moreover, as is seen in figure 4.8, the ability of these additives to supply sufficient electrolyte and to facilitate electron conduction to the electrochemically active surface is even more pronounced at the high discharge rates, where an increase from an improvement of 20% in capacity at low discharge rates improved to a difference of 74% in the 2X ZCC electrodes. The difference between the control and the zeolite-enhanced NAM indicates that as the rate of discharge is increased, the importance of the rate of supply of fresh electrolyte to the

surface becomes more and more impacting, resulting in a higher rate of reduction in capacity of the control material as compared to active material containing a hydrophilic additive, like zeolite Na-Y. The significantly larger change in capacity for active material containing hydrophilic and conductive additives demonstrates the importance of such a combination on the improvement in capacity at various rates of discharge. It should be noted that the C/4 rate displayed an anomalous behavior with respect to the other data points and was therefore not displayed.

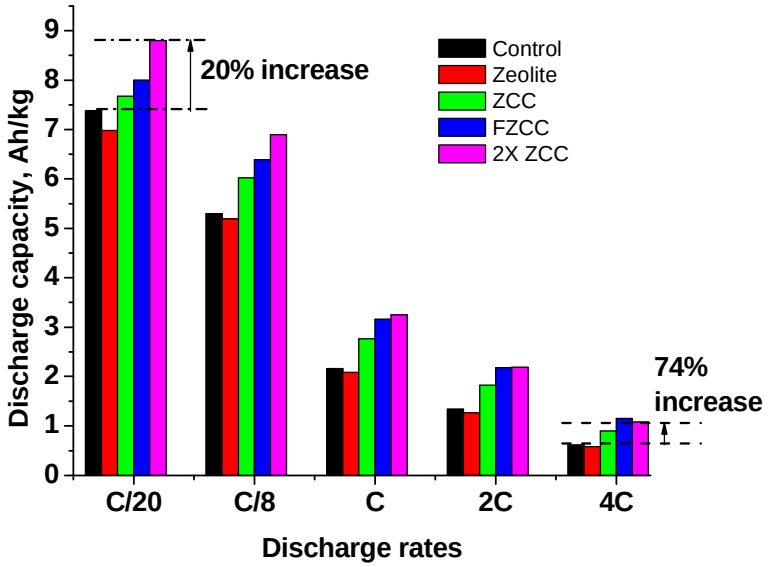

Figure 4.7. Capacities of LABs at different discharge rates as affected by the studied additives. The benefit of a hydrophilic and conductive additive is even more strongly demonstrated at high current rates with respect to active material utilization.

4.3.2 Static-Charge Acceptance Test

The SCA test provides a means to probe the ability of a cell to accept charge, or current, under an applied potential at low temperatures. This test is done at low temperatures (0 ˚F) and at a partial SOC (80%). A potential is applied to the cold cell at a reduced SOC and the accepted current is then monitored. The initial current can be affected by the SOC, so the best indication of the cells charge acceptance can be observed

in the region of the plot approximating a plateau (10 minutes is standard). From the study (results shown in figure 4.9) it was found that the control has the lowest charge acceptance rate of any cell, while the ZCC and 2X ZCC have the highest charge acceptance rate. The current in this region is a function of the ability of the material to provide a high conduction rate of redox species to the surface and the electrochemically active surface area. The ability of ZCC and 2X ZCC to accept the highest level of charge is attributed to their high levels of BET SSA observed during the sorption studies that appear to comport with an increased electrochemically active surface area and their ability to conduct electric charge to the redox active sites.

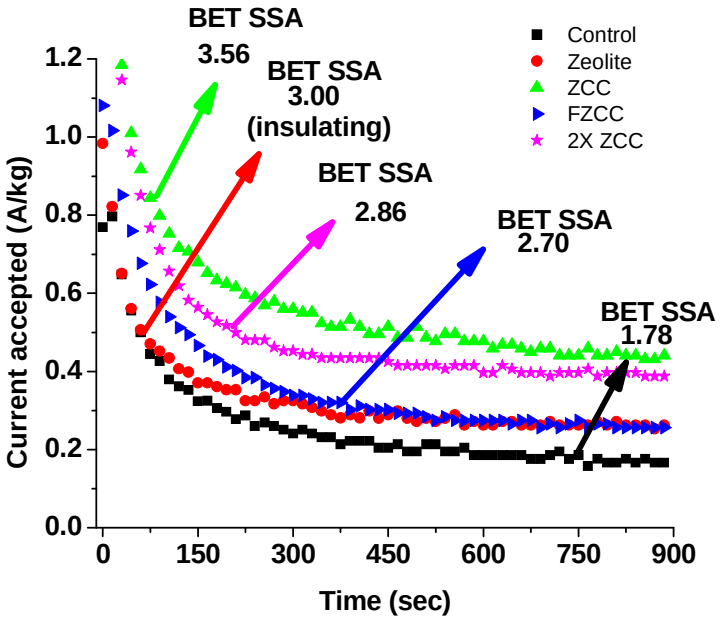

Figure 4.8. Charge acceptance characterization of LABs containing conducting/insulating hydrophilic additives. The current levels in the semi-plateau region provide insight into the kinetics of charge transfer, mass transport of redox species, and electrochemically active area of the active materials.

4.3.3 Power Density

The application of LABs in HEVs and EVs imposes a new set of electrochemically-based stressors on their materials, often requiring them to accept large

amounts of current and operate at a partial state of charge (HRPSOC). In order to qualify new materials for the advancement of LABs, a power density test is incorporated into the slew of electrochemical testing regimes. This test examines the current rates attainable by the LAB cell when a high discharge voltage is applied (2.67 V) at different SOC, in our case 80% and 60% SOC.

As figure 4.10 shows, the addition of a hydrophilic and conductive additive has clearly bested the control material. It appears that at extremely high discharge rates at partial states of charge, a hydrophilic additive, assisting in the transmission of redox species, does not allow for the proper conduction of electric charge to the necessary electrochemically active sites, facilitating the conversion of Pb and PbO_2 to lead sulfate. It seems that at extremely high rates, the need for sufficient electrolyte transmission through the additive itself (and its immediate surroundings) and conductivity become more prominent as compared lower rates. This is also seen for the ZCC additive. At these very high current rates, the SSA provided by ZCC is not a sufficient mitigating property to allow for high power density. The increased loading of 2X ZCC conductive additive permits higher conversion of active material to lead sulfate along with increased fresh electrolyte transmission. In the case of FZCC, the increased performance over ZCC is attributed to an increased affinity for the electrolyte stemming from the functionalization of the ZCC in sulfuric acid facilitating a higher rate of electrolyte conduction at the elevated current rates.

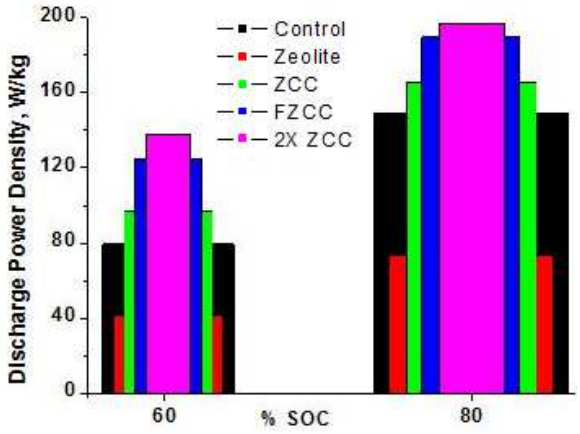

Figure 4.9. Power test characterization of LABs comprising the novel composite particles and contrasted with the control. The novel particles all appear to increase the capacity of the LAB under extremely high current conditions and demonstrate that hydrophilicity is not a sufficient characteristic for high power density.

4.3.4 Cycle Life

In order to study LABs for applications in which they may be exposed to HRPSOC and repeated charge and discharge a cycle life test reflecting these conditions was applied to the materials containing the novel additives. The test discharged the cells to PSOC conditions (C/20 down to 60% SOC) and proceeded to charge and discharge the cells at 2C until a cut-off voltage of 0.4V was reached. The highest performance registered is shown in figure 4.11 and 4.12. Figure 4.11 displays a cycle life graph that has a shape typical for secondary batteries. The difference in performance is significant. The performance demonstrated shows the potential of the materials to obtain higher than 100% improvement over the standard materials. The benefits of adding materials that provide a conduction path for both fresh electrolyte and charge transport to sites of active material are extremely pronounced with the highest performing cells displaying an increase of over 2 fold with respect to number of cycles possible at HRPSOC conditions. It appears that the electrodes containing the largest amount of ZCC had the longest cycle life while interestingly the zeolite additives, despite its shortcoming in other

electrochemical studies was next in line. It seems that in the case of cycle life, the key issue may be transmission of electrolyte deeper into the active material and this was facilitated by having an excess of ZCC and a particle like zeolite that facilitated the transmission of electrolyte but did not facilitate the growth of lead sulfate due to its insulating nature.

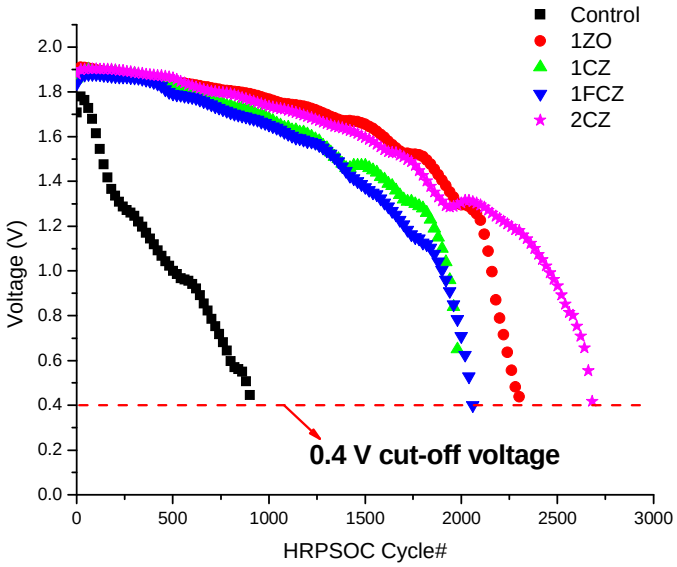

Figure 4.10. Voltage vs. number of charge-discharge cycles for the control and additive containing samples as derived from an HRPSOC simulating cycle life test.

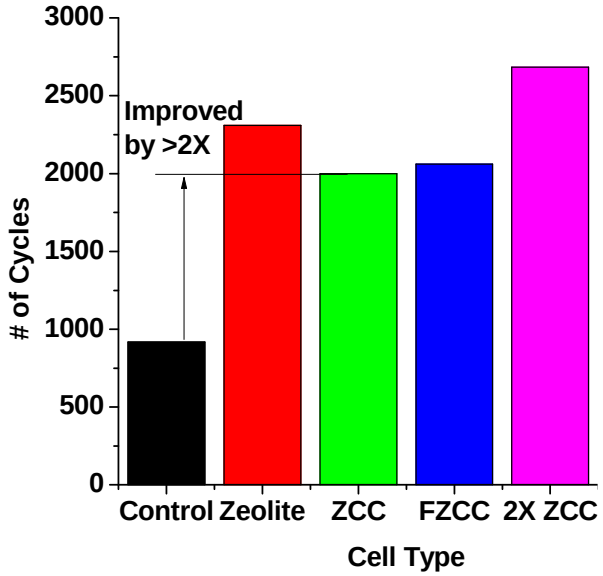

Figure 4.11. HRPSOC simulating cycle life test LABs consisting of the control materials, hydrophilic additives, and conductive hydrophilic additives. The test uses a 2C

rate charging and discharging around the 60% SOC. A clear improvement is demonstrated for all types of additives when cycle life is the target goal.

4.4 Conclusions

LABs have the potential to support the paradigm shift we are currently seeing with respect to the smart grid, renewable energy, and the enhanced electrification of our automobiles. In order to incorporate them, the design of their electrode materials must change. The design changes must allow for the operation of the LABs in a variety of states, most importantly at HRPSOC for efficient storage and rapid response to various activities like regenerative breaking and hybrid electric powertrain assistance [199].

The studies discussed in this chapter suggest that by using a small amount of additives in current lead-acid battery formulations may result in better LAB performance under the necessary conditions. In order to address the loss of contact with active material through the electrochemical conversion of the active material to insulating lead sulfate, a conductive and hydrophilic particle was designed and the first study implementing a zeolite-carbon composite particle in a LAB was carried out. The hydrophilicity of the particle was of key interest in order to examine its ability to further utilize active material through the conduction of electrolyte species to the active surfaces. These materials were shown to improve the performance of LAB as compared to standard formulations, in every test conducted, and likely in every respect necessary for a LAB to succeed in HRPSOC applications. A large increase in performance was seen in LABs incorporating the materials with respect to capacity (energy density) at slow and high rates, charge acceptance, power density, and cycle life. As templated carbons were previously stated to be hydrophobic, the desired characteristic of hydrophilicity by partial zeolite removal was studied. The hydrophilicity of the particles was demonstrated by examining moisture

retention and adsorption of water, through TGA and water sorption tests. The addition of these materials increased the BET surface area of the NAM and resulted in a charge acceptance improvement as high as ~2.5 times the control's current flow at the semi-plateau state. The capacity of the LABs was increased through an increase in active material utilization facilitated by a conduction path built by the conductive particle and a supply of electrolyte due to their hydrophilic nature and functionalized surfaces. This resulted in increases as high as 20% at low current rates and 75% at high current rates. These electron conduction paths and electrolyte transmission sites also resulted in large increases in power density and cycle life, all important features for the proliferation of LABs in advanced applications.

The improvements over standard LAB materials from a single dual-function particle, combining a hydrophilic and conductive nature, as well as a stable template dictating the morphology and pore size, is extremely promising and as the first study to focus on this novel design, opens the door for many further breakthroughs in LAB additive design and improvement and the incorporation of LABs in such important applications as the smart grid, industrial equipment, and mild to full electric vehicles.

CHAPTER 5

SUMMARY AND FUTURE WORK

The political and environmental state of the world at the moment is fueling significant change in the way we view our sources of energy and how we intend on utilizing them. Electrochemical energy storage is being sought for a vast array of applications, including an improved infrastructure for electrical energy generation and transmission (often referred to as the smart grid), and our automobiles. At the moment there are already electrochemical energy storage devices being used in air and ground vehicles and for the storage of renewable energy. In order to expand and maintain the use of such technologies, continued advancement is a necessity for both economic and feasibility reasons. In addition, in order to satiate our scientific curiosity and provide for more efficient advancements, a better understanding of the underlying mechanisms of these electrochemical energy storage systems is necessary. These notions are the impetuses for the work discussed in this thesis.

The electrochemical capacitor work discussed in this thesis was conducted to improve our understanding of the effect of pore size on the performance of ECs in low temperatures as well as contribute to the creation of ECs with improved performance. In order to better understand the effect of pore size and pore alignment a templated carbon with an ordered pore structure was synthesized by the decomposition of an organic precursor (acetylene) at low pressure on the inner surface of zeolite Na-Y powder. In addition, a novel electrolyte, consisting of SBP-BF_4 salt and an ACN:MF solvent mixture, was created that would allow for extending the operating temperature as compared to commercial $TEABF_4$ in ACN. The results were promising and insightful.

Through careful examination it was discovered that even seemingly purely ordered microporous carbons allow for the transmission and electroadsorption of ions at extremely low temperatures. In addition, an electrochemical capacitor was built that provided energy and power densities at extremely low temperatures on par with that of commercial devices at room temperature. This work has demonstrated the potential of properly tailoring the active material with the solvent, and specific ions interacting as part of the electroadsorption process. Further work needs to be done in order to find the optimal synthesis conditions for the carbons, annealing temperatures and time, and concentration of salt. As there are many solvents and salts available for use in electrochemical capacitors, further investigations of various combinations may lead to an extension of the lower operating limit. Investigations of the upper operating temperature need to be incorporated into future studies so as to provide a better understanding of the limits for these devices.

The lead-acid battery project discussed in this thesis has led to some very exciting results. Firstly, through the design of a particle providing conductivity, hydrophilicity, and a template-dictated structure, major increases in performance were observed. The additives were shown to provide enhancement in charge acceptance, capacity, power density, and cycle life, all of importance to applications in areas such as HEVs and renewable energy storage. Although, it seems fairly clear that hydrophilicity and conductivity are important characteristics for a particle to confer such benefits, future studies are necessary to advance our knowledge. In order to better understand the reasons behind the observed phenomena, further controlled studies needs to be undertaken. For future studies it is recommended that a longer deposition time of carbon be used (e.g.,

700 ˚C for 4 hours), which has previously shown promise in ECs. Then, subsequent activation times should be imposed so as to gradually increase the pore sizes followed by a surface cleaning treatment. A separate group of particles, similarly formed, should then undergo a functionalization treatment to increase their affinity to the electrolyte. This should provide a set of hydrophobic carbons with gradually modified pore structure, and hydrophilic carbons with gradually modified pore structure. They should then be incorporated at different wt. % and examine the resulting NAM's pore structure. In addition, different methods for mixing the materials may provide better dispersal of the particles throughout the NAM, and this is a key parameter to study as well. Studies should focus on examining the structure immediately in the vicinity of the novel additives and the dispersion of particles throughout the matrix. With further studies, such as the ones described, more information can be extracted on the intricate material system of the LAB and future advances, both scientific and technological, may be acquired.

REFERENCES

[1] H. Malmberg, Royal Institute of Technology, Stockholm 2007.

[2] H. G. Sarmiento, E. Estrada, Ieee Industry Applications Magazine 1996, 2, 16.

[3] D. R. Rolison, L. F. Nazar, Mrs Bulletin 2011, 36, 486.

[4] P. F. Ribeiro, B. K. Johnson, M. L. Crow, A. Arsoy, Y. L. Liu, Proceedings of The Ieee 2001, 89, 1744.

[5] P. Sharma, T. S. Bhatti, Energy Conversion And Management 2010, 51, 2901.

[6] M. Conte, Fuel Cells 2010, 10, 806.

[7] P. P. Barker, "Ultracapacitors For Use In Power Quality And Distributed Resource Applications", Presented At *Power Engineering Society Summer Meeting, 2002 Ieee,* 2002.

[8] P. T. Moseley, Journal of Power Sources 2009, 191, 134.

[9] J. R. C. Chien, K. C. Tseng, B. Y. Yan, Rev. Sci. Instrum. 2011, 82.

[10] P. Taylor, P. Butler, W. Nerbun, Journal of Power Sources 1997, 67, 187.

[11] P. Simon, Y. Gogotsi, Nature Materials 2008, 7, 845.

[12] J. R. Miller, A. F. Burke, Interface 2008, 17, 53.

[13] J. S. Cloyd, Ieee Aerospace And Electronic Systems Magazine 1998, 13, 17.

[14] C. H. Hamann, A. Hamnett, W. Vielstich, *Electrochemistry / Carl H. Hamann, Andrew Hamnett, Wolf Vielstich*, Wiley-Vch, Weinheim ; New York 1998.

[15] D. R.M, Solid State Ionics 2000, 134, 139.

[16] R. Ponraj, S. D. Mcallister, I. F. Cheng, D. B. Edwards, Journal of Power Sources 2009, 189, 1199.

[17] P. T. Moseley, B. Bonnet, A. Cooper, M. J. Kellaway, Journal of Power Sources 2007, 174, 49.

[18] M. Calabek, K. Micka, P. Krivak, P. Baca, Journal of Power Sources 2006, 158, 864.

[19] G. Toussaint, L. Torcheux, J. Alzieu, J. C. Camps, D. Livigni, J. F. Sarrau, J. P. Vaurijoux, D. Benchetrite, V. Gauthier, M. Vilasi, Journal of Power Sources 2005, 144, 546.

[20] S. D. Mcallister, S. N. Patankar, I. F. Cheng, D. B. Edwards, Scripta Materialia 2009, 61, 375.

[21] T. Robbins, J. M. Hawkins, "Powering Telecommunications Network Interfaces Using Photovoltaic Cells And Supercapacitors", Melbourne, Aust, 1997.

[22] T. Kyotani, T. Nagai, S. Inoue, A. Tomita, Chemistry of Materials 1997, 9, 609.

[23] P. Enzel, T. Bein, Chemistry of Materials 1992, 4, 819.

[24] P. Enzel, J. J. Zoller, T. Bein, Journal of The Chemical Society, Chemical Communications 1992.

[25] T. Cordero, P. A. Thrower, L. R. Radovic, Carbon 1992, 30, 365.

[26] H. I. Becker, *Usa Patent 2,800,616*, 1975.

[27] R. A. Rightmire, *Usa Patent 3,288,641*, 1966.

[28] S. Trasatti, G. Buzzanca, Journal of Electroanalytical Chemistry 1971, 29, A1.

[29] B. E. Conway, *Electrochemical Supercapacitors : Scientific Fundamentals And Technological Applications*, Plenum Press, New York : 1999.
[30] M. J. Sparnaay, *The Electrical Double Layer*, Pergamon Press, Oxford 1972.
[31] P. Kurzweil, Journal of Power Sources 2010, 195, 4424.
[32] C. Suozzo, In *Electrical Engineering*, Ohio State University, 2008.
[33] B. D, Journal of Power Sources 2001, 95, 2.
[34] C. M. Garner, G. Kloster, G. Atwood, L. Mosley, A. C. Palanduz, "Challenges For Dielectric Materials In Future Integrated Circuit Technologies", 2005.
[35] Vol. 2009, Wikimedia Commons, Capacitor Illustration.
[36] In *Electrochemistry Encyclopedia 2006*, Vol. 2009.
[37] W. D. Kingery, *Introduction To Ceramics*, Wiley, New York : 1976.
[38] M. A. T. Endo, T And Kim, Y. J. And Ishii, K., Carbon Science 2001, 1, 117.
[39] G. L. Bullard, H. B. Sierra-Alcazar, H. L. Lee, J. L. Morris, Magnetics, Ieee Transactions On 1989, 25, 102.
[40] N. A. Choudhury, A. K. Shukla, S. Sampath, S. Pitchumani, Journal of The Electrochemical Society 2006, 153, A614.
[41] A. Burke, Journal of Power Sources 2000, 91, 37.
[42] P. Simon, A. Burke, Interface 2008, 17, 38.
[43] E. Frackowiak, F. Beguin, Carbon 2001, 39, 937.
[44] L. Ionix Power Systems, Vol. 2009, Ionix Power Systems, Llc Electrochemical Capacitors.
[45] J. A. Banner, C. S. Winchester, "Rechargeable Lithium Batteries In The Navy - Policy And Protocol", Washington, Dc, Usa, 1996.
[46] H. Helmholtz, Annalen Der Physik 1853, 89, 211.
[47] G. Gouy, Annals of Physics 1917, 7, 129.
[48] D. L. Chapman, Philosophy Magazine 1913, 25, 475.
[49] O. Stern, Zeit Elektrochem 1924, 30, 508.
[50] D. C. Grahame, Chemical Reviews 1947, 41, 441.
[51] X. W. Huang, Z. W. Xie, X. Q. He, H. Z. Sun, C. Y. Tong, D. M. Xie, "Electric Double Layer Capacitors Using Activated Carbon Prepared From Pyrolytic Treatment of Sugar As Their Electrodes", 2003.
[52] W. M. Qiao, Y. Korai, I. Mochida, Y. Hori, T. Maeda, Carbon 2002, 40, 351.
[53] J. S. Im, S. W. Woo, M. J. Jung, Y. S. Lee, Journal of Colloid And Interface Science 2008, 327, 115.
[54] P. X. Han, C. Y. Wang, Z. Q. Shi, J. H. Lu, J. Qin, G. F. Yao, Journal of Inorganic Materials 2007, 22, 1046.
[55] W. M. Qiao, S. H. Yoon, I. Mochida, Energy & Fuels 2006, 20, 1680.
[56] Y. D. He, H. B. Liu, H. B. Zhang, New Carbon Materials 2002, 17, 18.
[57] X. H. Zeng, D. C. Wua, R. M. Fu, H. J. Lai, Materials Chemistry And Physics 2008, 112, 1074.
[58] C. X. Zhang, D. H. Long, B. L. Xing, W. M. Qiao, R. Zhang, L. Zhan, X. Y. Liang, L. C. Ling, Electrochemistry Communications 2008, 10, 1809.

[59] W. B. Xing, J. S. Xue, T. Zheng, A. Gibaud, J. R. Dahn, Journal of The Electrochemical Society 1996, 143, 3482.
[60] G. T. K. Fey, K. L. Chen, Y. C. Chang, Materials Chemistry And Physics 2002, 76, 1.
[61] G. T. K. Fey, D. C. Lee, Y. Y. Lin, T. P. Kumar, Synthetic Metals 2003, 139, 71.
[62] Q. Y. Li, H. Q. Wang, Q. F. Dai, J. H. Yang, Y. L. Zhong, Solid State Ionics 2008, 179, 269.
[63] V. V. N. Obreja, "On The Performance of Supercapacitors With Electrodes Based On Carbon Nanotubes And Carbon Activated Material - A Review", 2008.
[64] Z. X. Yang, Y. D. Xia, R. Mokaya, Journal of The American Chemical Society 2007, 129, 1673.
[65] M. Sevilla, S. Alvarez, T. A. Centeno, A. B. Fuertes, F. Stoeckli, Electrochimica Acta 2007, 52, 3207.
[66] C. Vix-Guterl, S. Saadallah, K. Jurewicz, E. Frackowiak, M. Reda, J. Parmentier, J. Patarin, F. Beguin, "Supercapacitor Electrodes From New Ordered Porous Carbon Materials Obtained By A Templating Procedure", 2004.
[67] A. B. Fuertes, F. Pico, J. M. Rojo, Journal of Power Sources 2004, 133, 329.
[68] I. H. Kim, J. H. Kim, B. W. Cho, K. B. Kim, Journal of The Electrochemical Society 2006, 153, A1451.
[69] W. C. Fang, Journal of Physical Chemistry C 2008, 112, 11552.
[70] C. Portet, G. Yushin, Y. Gogotsi, Carbon 2007, 45, 2511.
[71] V. V. Panic, R. M. Stevanovic, V. M. Jovanovic, A. B. Dekanski, "Electrochemical And Capacitive Properties of Thin-Layer Carbon Black Electrodes", 2008.
[72] S. L. Kuo, N. L. Wu, Journal of Power Sources 2006, 162, 1437.
[73] T. Osaka, X. J. Liu, M. Nojima, Journal of Power Sources 1998, 74, 122.
[74] K. Naoi, P. Simon, Interface 2008, 17, 34.
[75] G. Salitra, A. Soffer, L. Eliad, Y. Cohen, D. Aurbach, Journal of The Electrochemical Society 2000, 147, 2486.
[76] M. Endo, T. Maeda, T. Takeda, Y. J. Kim, K. Koshiba, H. Hara, M. S. Dresselhaus, Journal of The Electrochemical Society 2001, 148, A910.
[77] E. Raymundo-Piã±Ero, K. Kierzek, J. Machnikowski, F. Bã©Guin, Carbon 2006, 44, 2498.
[78] J. Chmiola, G. Yushin, Y. Gogotsi, C. Portet, P. Simon, P. L. Taberna, Science 2006, 313, 1760.
[79] Z. X. Ma, T. Kyotani, A. Tomita, Chemical Communications 2000, 2365.
[80] S. C. Pang, M. A. Anderson, T. W. Chapman, Journal of The Electrochemical Society 2000, 147, 444.
[81] J. P. Zheng, P. J. Cygan, T. R. Jow, Journal of The Electrochemical Society 1995, 142, 2699.
[82] J. W. Long, K. E. Swider, C. I. Merzbacher, D. R. Rolison, "Voltammetric Characterization of Ruthenium Oxide-Based Aerogels And Other Ruo2 Solids: The Nature of Capacitance In Nanostructured Materials", 1999.

[83] A. Chu, P. Braatz, Journal of Power Sources 2002, 112, 236.
[84] A. A. F. Grupioni, E. Arashiro, T. A. F. Lassali, Electrochimica Acta 2002, 48, 407.
[85] M. Wohlfahrt-Mehrens, J. Schenk, P. M. Wilde, E. Abdelmula, P. Axmann, J. Garche, "New Materials For Supercapacitors", 2002.
[86] J. P. Zheng, T. R. Jow, Journal of The Electrochemical Society 1995, 142, L6.
[87] S.-E. Chun, S.-I. Pyun, G.-J. Lee, Electrochimica Acta 2006, 51, 6479.
[88] P. Sivaraman, S. K. Rath, V. R. Hande, A. P. Thakur, M. Patri, A. B. Samui, Synthetic Metals 2006, 156, 1057.
[89] J. H. Park, O. O. Park, Journal of Power Sources 2002, 111, 185.
[90] K. H. An, K. K. Jeon, J. K. Heo, S. C. Lim, D. J. Bae, Y. H. Lee, Journal of The Electrochemical Society 2002, 149, A1058.
[91] M. Hughes, G. Z. Chen, M. S. P. Shaffer, D. J. Fray, A. H. Windle, Chemistry of Materials 2002, 14, 1610.
[92] C. F. Zhou, S. Kumar, C. D. Doyle, J. M. Tour, Chemistry of Materials 2005, 17, 1997.
[93] B. Monahov, D. Pavlov, A. Kirchev, S. Vasilev, Journal of Power Sources 2003, 113, 281.
[94] E. E. Ferg, In *Chemistry*, Vol. Doctor Technologiae, Port Elizabeth Technikon, Port Elizabth, South Africa 2004.
[95] D. R. Lide, *Crc Handbook of Chemistry And Physics, 88th Edition*, Crc, 2007-2008.
[96] L. Bonnefoi, P. Simon, J. F. Fauvarque, C. Sarrazin, J. F. Sarrau, P. Lailler, Journal of Power Sources 1999, 83, 162.
[97] J. P. Zheng, Z. N. Jiang, Journal of Power Sources 2006, 156, 748.
[98] R. Gallay, Vol. 2012.
[99] A. Lewandowski, M. Zajder, E. Frackowiak, F. Beguin, Electrochimica Acta 2001, 46, 2777.
[100] X. J. Liu, T. Osaka, Journal of The Electrochemical Society 1996, 143, 3982.
[101] F. Trinidad, F. Sáez, J. Valenciano, Journal of Power Sources 2001, 95, 24.
[102] O. Batteries, Vol. 2012.
[103] Onedirt, Vol. 2012.
[104] S. Pylypenko, T. S. Olson, N. J. Carroll, D. N. Petsev, P. Atanassov, Journal of Physical Chemistry C 2010, 114, 4200.
[105] J. H. Kim, J. S. Yu, Physical Chemistry Chemical Physics 2010, 12, 15301.
[106] B. Liu, S. Creager, Electrochimica Acta 2010, 55, 2721.
[107] D. Banham, F. X. Feng, T. Furstenhaupt, K. Pei, S. Y. Ye, V. Birss, Journal of Power Sources 2011, 196, 5438.
[108] J. B. Joo, P. Kim, W. Kim, J. Yi, Journal of Electroceramics 2006, 17, 713.
[109] C. O. Ania, V. Khomenko, E. Raymundo-Pinero, J. B. Parra, F. Beguin, Advanced Functional Materials 2007, 17, 1828.

[110] G. Y. Liu, Y. N. Li, J. M. Guo, B. S. Wang, In *Smart Materials And Intelligent Systems, Pts 1 And 2*, Vol. 143-144 (Eds: H. Wang, B. J. Zhang, X. Z. Liu, D. Z. Luo, S. B. Zhong), 2011, 749.
[111] A. B. Fuertes, G. Lota, T. A. Centeno, E. Frackowiak, Electrochimica Acta 2005, 50, 2799.
[112] M. Jung, H. G. Kim, J. K. Lee, O. S. Joo, S. Mho, Electrochimica Acta 2004, 50, 857.
[113] Q. A. Li, R. R. Jiang, Y. Q. Dou, Z. X. Wu, T. Huang, D. Feng, J. P. Yang, A. S. Yu, D. Y. Zhao, Carbon 2011, 49, 1248.
[114] S. Wen, M. Jung, O. S. Joo, S. I. Mho, Current Applied Physics 2006, 6, 1012.
[115] S. Wen, S. I. Mho, I. H. Yeo, Journal of Power Sources 2006, 163, 304.
[116] A. Kajdos, A. Kvit, F. Jones, J. Jagiello, G. Yushin, Journal of The American Chemical Society 2010, 132, 3252.
[117] N. Alam, R. Mokaya, Microporous And Mesoporous Materials 2011, 142, 716.
[118] Y. D. Xia, R. Mokaya, D. M. Grant, G. S. Walker, Carbon 2011, 49, 844.
[119] Y. X. Yang, C. M. Brown, C. X. Zhao, A. L. Chaffee, B. Nick, D. Y. Zhao, P. A. Webley, J. Schalch, J. M. Simmons, Y. Liu, J. H. Her, C. E. Buckley, D. A. Sheppard, Carbon 2011, 49, 1305.
[120] L. Wei, G. Yushin, Journal of Power Sources 2011, 196, 4072.
[121] J. Chmiola, G. Yushin, Y. Gogotsi, C. Portet, P. Simon, Science 2006, 313, 1760.
[122] H. Nishihara, H. Itoi, T. Kogure, P. X. Hou, H. Touhara, F. Okino, T. Kyotani, Chemistry-A European Journal 2009, 15, 5355.
[123] Sen-I Gakkaishi 2006, 62, P35.
[124] W. Li, J. Zhou, W. Xing, S. P. Zhuo, Y. M. Lu, Acta Physico-Chimica Sinica 2011, 27, 620.
[125] H. A. Xu, Q. M. Gao, H. L. Guo, H. L. Wang, Microporous And Mesoporous Materials 2010, 133, 106.
[126] C. Portet, Z. Yang, Y. Korenblit, Y. Gogotsi, R. Mokaya, G. Yushin, Journal of The Electrochemical Society 2009, 156, A1.
[127] H. L. Wang, Q. M. Gao, J. Hu, Microporous And Mesoporous Materials 2010, 131, 89.
[128] H. L. Wang, Q. M. Gao, J. Hu, Z. Chen, Carbon 2009, 47, 2259.
[129] R. Kotz, M. Hahn, R. Gallay, "Temperature Behavior And Impedance Fundamentals of Supercapacitors", 2006.
[130] S. Brunauer, P. H. Emmett, E. Teller, Journal of The American Chemical Society 1938, 60, 309.
[131] P. Webb, C. Orr, C. Micromeritics Instrument, *Analytical Methods In Fine Particle Technology*, Micromeritics Instrument Corporation, Norcross, Ga. 1997.
[132] J. Moore, Institute of Physics, 2001.
[133] Encyclopædia Britannica, Inc., 2009, Scanning Electron Microscope.
[134] B. Fultz, J. M. Howe, Springerlink, *Transmission Electron Microscopy And Diffractometry of Materials [Electronic Resource] / Brent Fultz, James Howe*, Springer, Berlin ; New York 2008.

[135] Vol. 2012, 2009, Diagram Outlining The Internal Components of A Basic Tem System.
[136] K. N. Casper, Natural Resources Journal 2010, 49, 825.
[137] J. S. Lawrence, M. C. B. Ashley, S. Hengst, D. M. Luong-Van, J. W. V. Storey, H. Yang, X. Zhou, Z. Zhu, Rev. Sci. Instrum. 2009, 80, 10.
[138] J. P. Matthews, A. J. Smith, I. D. Smith, Planetary And Space Science 1979, 27, 1391.
[139] J. A. Rosero, J. A. Ortega, E. Aldabas, L. Romeral, Ieee Aerospace And Electronic Systems Magazine 2007, 22, 3.
[140] C. R. Sides, C. R. Martin, Adv. Mater. 2005, 17, 125.
[141] S. S. Zhang, K. Xu, T. R. Jow, Electrochim. Acta 2004, 49, 1057.
[142] J. R. Miller, P. Simon, Science 2008, 321, 651.
[143] W. C. West, M. C. Smart, E. J. Brandon, L. D. Whitcanack, G. A. Plett, Journal of The Electrochemical Society 2008, 155, A716.
[144] E. J. Brandon, W. C. West, M. C. Smart, L. D. Whitcanack, G. A. Plett, Journal of Power Sources 2007, 170, 225.
[145] I. Kovalenko, D. Bucknall, G. Yushin, Adv. Funct. Mater. 2010, Doi: 10.1002/Adfm.201000906.
[146] J. Li, I. Zhitomirsky, Colloids And Surfaces A-Physicochemical And Engineering Aspects 2009, 348, 248.
[147] T. R. Jow, J. P. Zheng, J. Electrochem. Soc. 1998, 145, 49.
[148] D. Hulicova-Jurcakova, M. Seredych, G. Q. Lu, T. J. Bandosz, Adv. Funct. Mater. 2009, 19, 438.
[149] D. Hulicova-Jurcakova, M. Kodama, S. Shiraishi, H. Hatori, Z. H. Zhu, G. Q. Lu, Adv. Funct. Mater. 2009, 19, 1800.
[150] L. Wei, M. Sevilla, A. B. Fuertesc, R. Mokaya, G. Yushin, Advanced Energy Materials 2011, Accepted.
[151] M. Rose, Y. Korenblit, E. Kockrick, L. Borchardt, M. Oschatz, S. Kaskel, G. Yushin, Small 2011.
[152] Y. Korenblit, M. Rose, E. Kockrick, L. Borchardt, A. Kvit, S. Kaskel, G. Yushin, Acs Nano 2010, 4, 1337.
[153] A. Kajdos, A. Kvit, F. Jones, J. Jagiello, G. Yushin, J. Am. Chem. Soc. 2010, 132, 3252.
[154] B. E. Conway, *Electrochemical Supercapacitors*, Vol. 1, Kluwer Academic / Plenum Publishers, New York 1999.
[155] M. Rose, Y. Korenblit, E. Kockrick, L. Borchardt, M. Oschatz, S. Kaskel, G. Yushin, Small 2011.
[156] C. G. Liu, Z. N. Yu, D. Neff, A. Zhamu, B. Z. Jang, Nano Letters 2010, 10, 4863.
[157] C. Portet, G. Yushin, Y. Gogotsi, J. Electrochem. Soc 2008, 155 (7).
[158] D. Pech, M. Brunet, H. Durou, P. H. Huang, V. Mochalin, Y. Gogotsi, P. L. Taberna, P. Simon, Nature Nanotechnology 2010, 5, 651.
[159] J. R. Miller, R. A. Outlaw, B. C. Holloway, Science 2010, 329, 1637.
[160] C. S. Du, J. Yeh, N. Pan, Nanotechnology 2005, 16, 350.
[161] C. Portet, P. L. Taberna, P. Simon, E. Flahaut, C. Laberty-Robert, Electrochim. Acta 2005, 50, 4174.

[162] J. Gamby, P. L. Taberna, P. Simon, J. F. Fauvarque, M. Chesneau, Journal of Power Sources 2001, 101, 109.
[163] E. Raymundo-Pinero, K. Kierzek, J. Machnikowski, F. Beguin, Carbon 2006, 44, 2498.
[164] J. S. Huang, B. G. Sumpter, V. Meunier, Angewandte Chemie-International Edition 2008, 47, 520.
[165] J. S. Huang, B. G. Sumpter, V. Meunier, Chemistry-A European Journal 2008, 14, 6614.
[166] J. Chmiola, G. Yushin, R. K. Dash, E. N. Hoffman, J. E. Fischer, M. W. Barsoum, Y. Gogotsi, Electrochemical And Solid State Communications 2005, 8 A357.
[167] E. N. Hoffman, G. Yushin, T. El-Raghy, Y. Gogotsi, M. W. Barsoum, Microporous Mesoporous Mater. 2008, 112, 526.
[168] G. Yushin, R. K. Dash, Y. Gogotsi, J. Jagiello, J. E. Fischer, Adv. Funct. Mater. 2006, 16, 2288.
[169] C. Portet, G. Yushin, Y. Gogotsi, J. Electrochem. Soc 2008, 155 (7), A531.
[170] R. T. Yang, *Adsorbents: Fundamentals And Applications*, Wiley & Sons, Inc., Hoboken, Nj, Usa 2003.
[171] K. Chiba, T. Ueda, H. Yamamoto, Electrochemistry 2007, 75, 664.
[172] S. W. Lee, N. Yabuuchi, B. M. Gallant, S. Chen, B.-S. Kim, P. T. Hammond, Y. Shao-Horn, Nat Nano 2010, 5, 531.
[173] G. Feng, R. Qiao, J. S. Huang, B. G. Sumpter, V. Meunier, Acs Nano 2010, 4, 2382.
[174] J. S. Huang, B. G. Sumpter, V. Meunier, G. Yushin, C. Portet, Y. Gogotsi, Journal of Materials Research 2010, 25, 1525.
[175] D. W. Wang, F. Li, M. Liu, G. Q. Lu, H. M. Cheng, Angewandte Chemie-International Edition 2008, 47, 373.
[176] P. L. Taberna, P. Simon, J. F. Fauvarque, Journal of The Electrochemical Society 2003, 150, A292.
[177] J. O. M. B. A. A. K. N. Reddy, *Modern Electrochemistry 1: Ionics, 2nd Edition*, Plenum Press, New York 1998.
[178] J. Szymborski, "Lead-Acid Batteries For Use In Submarine Applications", Presented At *Autonomous Underwater Vehicles, 2002. Proceedings of The 2002 Workshop On*, 2002, 2002.
[179] W. Rainer, Journal of Power Sources 2005, 144, 494.
[180] H. A. Catherino, F. F. Feres, F. Trinidad, Journal of Power Sources 2004, 129, 113.
[181] J. Timmons, R. Kurian, A. Goodman, W. R. Johnson, Journal of Power Sources 2004, 136, 372.
[182] B. G.H, Journal of Power Sources 1999, 78, 68.
[183] E. E. Ferg, P. Loyson, A. Poorun, Journal of Power Sources 2006, 155, 428.
[184] H. Dietz, J. Garche, K. Wiesener, Journal of Power Sources 1985, 14, 305.
[185] S. D. Mcallister, R. Ponraj, I. F. Cheng, D. B. Edwards, Journal of Power Sources 2007, 173, 882.

[186] P. T. Moseley, R. F. Nelson, A. F. Hollenkamp, Journal of Power Sources 2006, 157, 3.
[187] N. E. Bagshaw, Journal of Power Sources 1997, 67, 105.
[188] P. T. Moseley, Journal of Power Sources 1997, 64, 47.
[189] J. Valenciano, A. Sanchez, F. Trinidad, A. F. Hollenkamp, Journal of Power Sources 2006, 158, 851.
[190] A. Ferreira, J. Jordan, J. Wertz, G. Zguris, Journal of Power Sources 2004, 133, 39.
[191] M. A. Karimi, H. Karami, M. Mahdipour, Journal of Power Sources 2006, 160, 1414.
[192] D. R. Rolison, Chemical Reviews 1990, 90, 867.
[193] B. Hariprakash, S. A. Gaffoor, A. K. Shukla, Journal of Power Sources 2009, 191, 149.
[194] S. E. Afifi, A. E. Saba, A. Y. Shenouda, Journal of Power Sources 1993, 46, 285.
[195] R. J. Ball, R. Evans, E. L. Thacker, R. Stevens, Journal of Materials Science 2003, 38, 3013.
[196] M. K, Journal of Power Sources 1996, 59, 31.
[197] L. Ji, F. Liu, Z. Xu, S. Zheng, D. Zhu, Environmental Science & Technology 2009, 43, 7870.
[198] Y. Korenblit, A. Kajdos, W. C. West, M. C. Smart, E. J. Brandon, A. Kvit, J. Jagiello, G. Yushin, Advanced Functional Materials 2012, N/A.
[199] E. Karden, S. Ploumen, B. Fricke, T. Miller, K. Snyder, Journal of Power Sources 2007, 168, 2.